Influences of large fillets on endwall flows in a vane cascade with upstream slot film-cooling

Adeola S. Shote, Gazi I. Mahmood*, and Josua P. Meyer
Department of Mechanical and Aeronautical Engineering
University of Pretoria, Pretoria 0028, South Africa

*Corresponding author: gazi.mahmood@up.ac.za

ABSTRACT

Investigations in cascade employ filleted blades to influence the near endwall secondary flows and total-pressure losses. The secondary flows aggravate the aerodynamic losses and endwall thermal stresses in the gas turbine passages. Investigations of different configurations of the slot-bleed flow from the endwall of cascade upstream show significant influences on the near endwall flows. In the present paper, the near endwall flow-field in a linear cascade employing filleted vanes and bleed flow from the upstream endwall slots is measured experimentally. Two fillet profiles are tested, one is larger than the other. The objectives are to quantify the combined effects of endwall fillet, fillet profiles, and film-cooling flow on the endwall region flow-field. The fillet covers the junction of vane and endwall upstream of the cascade throat region. The discontinuous bleed-slots near the cascade entrance provide the film-cooling flow on endwall and simulate the gaps between combustor/nozzle-vane discs or stator/rotor discs in the gas turbine. The inlet Reynolds number of 2.0E+05 is based on the chord length of vane profile. The density and temperature ratios of the coolant flow to mainstream are both about 1.0. The inlet blowing ratio of the film-cooling flow varies between 1.0 and 2.8. The flow-field is measured through the distributions of flow temperature, yaw angle, axial vorticity, and total-pressure losses along the vane passage. The effects on the flow-field are then presented by comparing the cases of filleted vanes with the cases of un-filleted vanes. The results of flow yaw angle and axial vorticity in the filleted passage are smaller than those in the passage without the fillet. The yaw angles responsible for the endwall secondary flows are the smallest for the smaller fillet (Fillet-2). The temperature field indicates the pitchwise distributions of the coolant on endwall specially near the pressure side are better when the smaller fillet is employed. Also,

the weakened passage vortex of the endwall secondary flows in the filleted passage reduces the total-pressure losses. Although the total-pressure losses decrease at very high coolant mass flux with and without the fillet, the losses are always smaller for the filleted passage than for the un-filleted passage. The present investigation is beneficial for improving and optimizing the endwall film-cooling in the gas turbine passage.
Keywords: *Blowing ratio; Coolant mass flux; Flow deviation; Passage vortex; Pressure loss.*

1. Introduction

Aerodynamic losses, high heat transfer at endwall, and reduced film cooling effectiveness in the rotor and stator passages of gas turbine are primarily caused by the secondary flows in the endwall region. The high amount of film-cooling flow rate to control the high thermal stresses in the endwall causes the turbine efficiency to suffer. Filleted blades have been the subject of investigations to reduce the effects of endwall secondary flows. The geometry and configurations of the film-cooling holes also reduce the secondary flow losses in the cascade to some extent. The experimental work presented here investigates the flow and temperature fields in the endwall region of a cascade that employs vane-blades with extended fillet and a slot film-cooling configuration in the endwall at the cascade inlet. The objectives are to quantify the aerodynamic effects of the fillet on the endwall flows in the film-cooled passage. The temperature field indicates the effects on the coolant distributions on the endwall when the fillet is employed.

The structures of the secondary flows formed as the passage vortices in the endwall region and the resulting aerodynamic losses in the blade cascade passages are described by Ligrani et al. [1]. The filleted vane-blades and rotor-blades are employed by [2-10] to affect the endwall secondary flows and aerodynamic losses including the total-pressure losses and turbulent kinetic energy in the cascades. The large fillets in the investigations of [2-10] influence the flow angles, pitchwise pressure gradients, and turbulence in the cascade passages to change the locations, structures, and vorticity of the endwall secondary flows and to reduce the losses. The fillets of [2-10] are also responsible for the reduced endwall heat transfer. In contrast, the small fillets around the blade profile at endwall of [11, 12] enhance the secondary flow losses.

The film-cooling flows from the discrete holes in the cascade endwall employed by Thomas and Povey [13] and Salvadori et al. [14] enhance the aerodynamic losses across the passage. The film-cooling flows from the continuous slots of [15-19] simulate the leakage flow between two platforms or two mounting disks in the gas turbine. The results of [15-19] show the interactions of the coolant flows from

slots with the endwall flows intensify the passage vortex and secondary flow losses. However, the secondary flows in the vane cascade of [20-23] become weak with the film-cooling flows from the special slot geometry in the upstream endwall. The results of [20, 23] with the angled purge-cooling indicate the reduced flow turnings relative to the mid-span streamlines weaken the passage vortex and total-pressure losses at the cascade exit. Oke and Simonson [24] measure the temperature field to show the film-cooling flow distributions on the endwall with different arrangements of the slot bleed at the cascade inlet.

The effects of discrete hole film-cooling on the flow-field at cascade endwall employing small fillet at the blade-platform junction are shown by [25, 26]. The high mass-flux ratio of coolant to mainstream flow reduces the passage vortex and aerodynamic losses in Ornano and Povey [25], but shows little influences in Barigozzi et al. [26]. However, the film-coverage of the endwall increases with the coolant mass-flux ratio in both [25, 26]. The investigation of Zhang et al. [27] reports the film-cooling effectiveness on endwall in a filleted vane cascade. No flow-field data are presented by [27].

The past investigations in cascades emphasize the geometry and configurations of both the film-cooling holes in endwall and fillet at the blade-endwall junction affect the interactions between the coolant and endwall flows. The coolant flow trajectory, passage vortices and associated secondary flow losses, and coolant distributions on the cascade endwall are thus significantly influenced. However, the effects of large fillets on the film-cooled endwall flow-field and coolant distributions with the upstream slot-bleed flow in the cascade have not been investigated in detail. The flow results of slot-bleed in [23] are presented without the filleted vanes. Mahmood and Arnachellan [28] provide flow properties with the slot-bleed in a filleted vane cascade. The effects of fillet geometry on the results in [28] are absent. In the present experiment, a two-dimensional vane cascade employs discrete slots in the upstream endwall and a large fillet at the junction of vane and endwall. Two fillet profiles and a fixed slot geometry are tested at different film-cooling blowing or mass-flux ratios. The density and temperature ratios of the coolant to mainstream flow are kept constant. Both the fillets extend upstream to cover the film-cooling slots partially and extend downstream to reach the passage throat region. The effects on the flow-field and coolant distributions along the cascade passage are examined through the measurements of velocity components, flow angles, total-pressure, and temperature. The investigation is important for the endwall film-cooling design and reductions of secondary flow losses in the cascade leading to the energy efficient cooled blade passages.

2. Experimental set-up and methodology

Figure 1(a) shows the two-dimensional schematic of an atmospheric wind tunnel housing the linear cascade test section. The tunnel cross-section is rectangular. Two duct blowers of 15 kW and 7.5 kW

connected in series induct in the ambient air through the tunnel under suction. The main components of the tunnel leading to the cascade are a honeycomb-mesh screen combination at the inlet of a two-dimensional contraction, a turbulence grid of cylindrical rods, and a flow settling section. The tunnel walls are made of wood except the test section which is made of clear polycarbonate. Further details of the wind tunnel are provided in [29]. The seven vane-blades numbered as 1 to 7 in the cascade test section as shown in Fig. 1(a) are screwed to the endwalls. The two-dimensional vane is generated from the hub-side profile of the first stage guide-vane of the GE-E^3 turbine engine [29, 30]. The cascade geometry is scaled 6 times the actual guide-vane stage geometry. The geometric parameters employed by the cascade are provided in Table 1. The polycarbonate vane skin is coated with polyurethane for a smooth finish. The flow condition in the cascade passages is made periodic when some air flow is by-passed through the sides of the vane 1 and vane 7. The measurements are obtained in the shaded passages of vanes 3, 4, and 5 of Fig. 1(a). A cut-out slot in the top endwall at the reference plane location $2.5C_{ax}$ upstream of the cascade inlet is used to measure the reference properties. The passive turbulence grid is placed in the rectangular settling section at $4C_{ax}$ upstream of the reference plane. Figure 1(a) also shows the placement of the fillet at the junction of vane and endwall. Arnachellan [29] provides more geometric details of the wind tunnel and cascade test section.

Figure 1(b) shows the vane profile, locations and geometry of the film-cooling slots, and locations of the four measurement planes (planes-1 to 4). The local and global Cartesian coordinate systems for the measurements are also indicated in the figure. The coordinate origins are always located at the bottom endwall. The axial locations (X_G/C_{ax}) of the measurement planes in Fig. 1(b) are then the distances of the plane origins on the vane profile from the leading edge. Plane-1 and plane-2 are oriented normal to the vane profile while plane-3 and plane-4 are normal to the axial direction, X_G. Cut-out slots in the top endwall at the locations of measurement planes provide access of the flow measuring probes into the cascade passage. Four discrete film-cooling slots in the bottom endwall along the vane pitch are located $0.08C_{ax}$ upstream of the inlet of the cascade passage. As shown in Fig. 1(b), the two slots of length 82 mm each (pitchwise) are located directly upstream of the vane leading edge and the other two of length 55 mm each are located in the pitchwise middle position between the larger slots. The slot axial direction and length (L) are 30° and 40 mm, respectively, in the endwall. The geometry and location of the present endwall slots follow those of the continuous slots of [22. 24, 31, 32]. However, the present film-cooling slots are discontinuous to represent the densely populated multi-row film-cooling holes in the locations of the individual slots. The coolant streams from the holes in the immediate vicinity of the hole-exits combine and interact which can be simulated by a discontinuous slot. The blocked leakage-gaps between the turbine rims due to some residual deposits of the combustion gas can be also represented by the

discontinuous slots. Further, the previous studies show the coolant distributions downstream immediately of the exit of continuous slot are not uniform due to the pitchwise non-uniform pressure distributions on endwall. The discontinuous slots are employed in an effort to uniformly distribute the coolant as the streams approach the cascade inlet. Note that the measurement plane-4 in Fig. 1(b) is located about 7 mm upstream in reference to the exit plane in [23].

The profiles and geometry of the two fillets are shown in Fig. 1(c). Both the fillets cover the leading edge region with about the same maximum height, $(Y_G/S)_{Max}$ at the vane leading-edge. The maximum height, $(Y_G/S)_{Max}$ of the fillets is equivalent to the endwall boundary layer thickness of the incoming flow. The fillet height from the vane surface to endwall and from the fillet leading-edge to trailing-edge decreases linearly. The fillet profile thus blends smoothly with the vane and endwall at the trailing-edge. Fillet-1 profile is larger on the endwall than fillet-2. Also, the trailing-edge of fillet-1 extends to the passage throat locations on the vane pressure and suction sides while that of fillet-2 extends upto X_G/C_{ax} = 0.62 on both sides of the vane. The throat is also located at X_G/C_{ax} = 0.62 on the vane suction side. The profiles of both fillets around the vane follow the vane profile. The fillet is employed only at the bottom endwall as an add-on to the vane profile and is not instrumented for any pressure or temperature measurements. A 3-dimensional printer (stereo lithography) is used to manufacture the fillets.

Figure 2(a) shows the axial-locations of the four measurement planes-(1 to 4) along the vane passage and the film-cooling configurations with and without the fillets. The film-cooling slots are configured into four types based on the slot-opening area and fillet geometry employed: (i) baseline-1: all four slots open, no fillet employed, (ii) baseline-2: the 55 mm slots open, the 82 mm slots open 2% on pressure side and 22% open on suction side, no fillet employed, (iii) fillet-1: the 55 mm slots open, the 82 mm slots closed, fillet-1 employed, and (iv) fillet-2: the 55 mm slots open, the 82 mm slots open 2% on pressure side and 22% open on suction side, fillet-2 employed. The darkened parts of the 82 mm slots in the rightmost diagram of Fig. 2(a) indicate the blocked slots of configuration (ii). The slots are fully open in configuration (i). Table 2 summarizes the four types of slot openings.

Figure 2(b) shows the schematic of the flow circuit to deliver the film-cooling flow. Two blowers of 1.0 kW and 800 W in series deliver the film-cooling flow into a large plenum-box located beneath the film-cooling slots through a metered-pipe. The ISO (International Standard Organization) standard orifice plate in the pipe measures the mass flow rate of coolant flow. The flow temperature is controlled by the evaporator heat-exchanger (cooling coil) of a vapor-compression unit just upstream of the plenum. The wooden plenum-box and the passage endwall of the cascade are thermally insulated. The large volume of the plenum diffuses the turbulence and velocity in the coolant flow before it enters the film-cooling slots. Static pressure taps in the plenum walls are connected to a differential pressure transducer

to measure the total pressure of the coolant flow. The combinations of the blowers and diameters of the metered pipe and orifice plate in the flow circuit provide the required coolant mass flow and inlet blowing ratio. Equation (1) defines the inlet blowing ratio for the film-cooling flow. Arnachellan [29] provides more details of the cooling flow circuit in Fig. 2(b). During the temperature-field measurements, the film-cooling supply temperature, $T_{c,b}$ is maintained at about 6 °C. Thermocouples located in the plenum-box measure the coolant temperature.

$$\mathrm{M_{in}} = \sqrt{\frac{\mathrm{P_{t,b}} - \mathrm{P_{s,r}}}{\mathrm{P_{t,r}} - \mathrm{P_{s,r}}}} \tag{1}$$

Pressure tap holes of diameter 0.3 mm in the profiles of vanes 3, 4, and 5 (refer to Fig. 1) at the mid-span location provide measurements of the wall-static pressure distributions along the vane profile. The hollow core of the vane allows the plastic tubes connected to the pressure tapes to be routed out to a differential pressure transducer through a multi-port scanner [29]. The reference flow properties are measured by traversing a five-hole pressure probe and a hot-wire anemometer probe in the reference plane of Fig. 1(a) through the slot in the top endwall. The flow-fields in the planes-1 to 4 of Fig. 2(a) are scanned with the five-hole pressure probe and a temperature probe. The un-used slots in the top endwall are masked with plastic liners during the measurements. The measurement grid uses a spanwise (*Y*-direction) and pitchwise (*Z*-direction) resolutions of 2 or 4 mm and 3 or 5 mm, respectively. The spatial resolutions of the scans in the boundary and secondary flow regions are finer. The commercial five-hole pressure probe has a conical tip of diameter 1.6 mm. The temperature probe is made in-house from the K-type thermocouple of wire diameter of 0.25 mm. A pair of needle prongs 10 mm apart at the end of the temperature probe-stem holds the thermocouple tip. A pitot-static pressure probe and a thermocouple record the pressure, velocity, and temperature simultaneously at a fixed location in the reference plane as the five-hole pressure probe or temperature probe scans the planes in the passage. The pressure probes are connected to the differential pressure transducers. The data from the transducers are digitized via the National Instruments™ data loggers at 100 Hz for 200 samples for the pressures, at 60 Hz for 120 samples for the temperature, and at 5 kHz for 10 sec for the turbulence intensity. The recorded voltage data are then time-averaged and converted into the pressure unit of Pa, temperature unit of °C, and velocity unit of m/s after applying the appropriate calibrations. The calibration coefficients of the five-hole probe that determine the velocity components, flow angles, and pressures are provided in [29]. One single Labview™ program coded in-house records data from the data loggers and controls the probe traversing unit through a motor controller. The test passages of Fig. 1(a) are not instrumented for the

temperature measurements on the endwall in the present investigations. No data of the film-cooling effectiveness on endwall are available for the cases presented here.

The 95% confidence interval is used to estimate the uncertainties in the measured data. The uncertainties in the calculated data are estimated based on the propagation of errors of [33, 34]. The uncertainties in the reference velocity and pressure are 1.6% and 3.6%, respectively. The coefficient of static pressure has uncertainty of 5.7%. The maximum uncertainties in the total pressure and total pressure loss coefficient are 7% and 8.2%, respectively. The flow angles have the maximum uncertainty of 5%. The velocity and vorticity in the passage then have the maximum uncertainties of 8% and 11%, respectively. The maximum uncertainty in the film-cooling flow rate is 0.7% and in the inlet blowing ratio is 1.4%. The temperature and its non-dimensional form have uncertainties of 0.2 °C and 4%, respectively.

3. Discussions of results

The measurements are obtained at the atmospheric and adiabatic conditions at steady-state when the pressure and temperature in the test section vary by less than ±2 Pa and ±0.2 °C, respectively, over 10 minutes. The measured data are normalized with the reference properties in Table 3. The properties in the table are the averages of the local values obtained by scanning the reference plane with the probes. The local velocity and pressure change only by 0.2 m/s and 0.5 kPa, respectively, at the maximum. The freestream velocity and turbulence intensity in Table 3 are reported above the boundary layer of the bottom endwall. The coolant to reference temperature (absolute) ratio, $T_{c,b}/T_r$ is 1.0 for the flow measurements and 0.94 during the temperature field measurements. When no film-cooling flow (M_{in} = 0) is supplied, the slot openings are covered with tapes. The fillets and film-cooling slots are employed at the bottom endwall in the passages between vanes-3, 4, and 5. Data with the 55 mm slots open and 82 mm slots closed are presented in [23]. The flow properties in the baseline cascade [23] without the film-cooling and fillet are also not repeated as the present objectives are to investigate the fillet effects on the film-cooling flow. The film-cooling flow conditions and measurement locations in the present cases of baseline-1 and fillet-1 are somewhat different from those in [23, 28]. The distributions of local flow properties are presented in the following with the measurement locations shown in the three-dimensional passage view for clarity.

Figure 3 presents the pressure coefficients, $C_{p,blade}$ along the vane profile at the mid-span location of Y_G/S = 0.5. Equation (2) determines the $C_{p,blade}$ from the local pressure, $P_{s,b}$ on the vane profile. The data are measured without any film-cooling flow (M_{in} = 0). The coordinate on vane profile is given by s/C with the origin, s/C = 0 located at the leading edge (Fig. 1(b)). The comparisons of $C_{p,blade}$ distributions

among vanes-3 ,4, and 5 in Fig. 3(a) for the baseline case (no fillet and film-cooling) show no significant differences. The results confirm the periodic flow conditions in the measurement passages. The $C_{p,blade}$ distributions on vane-4 with the two fillets in Fig. 3(b) also compare reasonably well with those for the baseline indicating the flow periodicity with the fillet as well. The data on vanes-3 and 5 with the fillets are not presented for clarity of the plots in Fig. 3(b).

$$C_{p,blade} = \frac{(P_{s,b} - P_{s,r})}{(P_{t,r} - P_{s,r})} \tag{2}$$

The coolant stream distributions with local concentrations, coolant coverage on the endwall, and mixing of coolant streams with the endwall flows at the three measurement planes (planes-1 to 3) are shown by the distributions of non-dimensional temperature, θ in Figs. 4 to 7. Equation (3) defines θ using the measured air temperatures, T_a in the planes. The definition of θ in the equation refers to the temperature rise in the coolant stream, (T_a - $T_{c,b}$) relative to the maximum temperature rise, ($T_r - T_{c,b}$) as the coolant streams and endwall flows interact and mix. The high values and maximum of $\theta = 1$ are then caused by the flow mixing and lifting-up of the coolant streams by the endwall flows or as no presence of the coolant. The coolant stream temperature is unaffected when $\theta = 0$. The lower values of θ near the endwall also indicate the concentration of the coolant streams and are thus beneficial to the film-cooling coverage and adiabatic effectiveness. The coolant flow trajectories, in conjunction with the slot opening area, influence the distributions of low values of θ inside the incoming boundary layer i.e. $Y/S < 0.1$ in the plots of Figs. 4 to 7.

$$\theta = \frac{(T_a - T_{c,b})}{(T_r - T_{c,b})} \tag{3}$$

Figures 4 and 5 present the non-dimensional temperature, θ in plane-1 and plane-2, respectively, for $M_{in} = 2.2$ for the cases of film-cooling with and without the fillets. The locations of the planes in the three-dimensional passage, slot positions, and opening area of the slots for the different film-cooling configurations are also shown at the bottom of the plot area in the figures. The partially blocked slots of the baseline-2 configuration are fully open in the baseline-1 configuration. The shaded area at the bottom corner (left or right) of the contour plot for the fillet film-cooling identifies the filleted region. The spanwise axis, Y/S is shown on the right side of each plot in Fig. 4. Note that plane-1 and plane-2 are located in the travel path of pressure side-leg vortex and suction side-leg vortex, respectively. The vortex

legs and separated boundary layer lift up the coolant flows to mix with the endwall flows. The distributions of θ for the baseline-1, baseline-2, and fillet-2 are almost the same in Fig. 4 as well as in Fig. 5 indicating similar coolant trajectories and influences of the vortex structures in the three cases. For the baseline-1 in Fig. 4 at $Z/P < -0.15$ and in Fig. 5 at $Z/P < 0.12$, the θ distributions have slightly higher values and much less concentration of the coolant streams compared to the other cases because of no coolant flow from the 82 mm slots. The θ contours of Fig. 5 at $Z/P < 0.10$ near the SS for the baseline-1 show some concentration of the coolant streams from the leading edge slot (82 mm slot). As the leading edge slot is partially blocked for the baseline-2 and fillet-2, the coolant is lifted-up by the suction side-leg vortex at $Z/P < 0.10$ in Fig. 5 causing the $\theta < 0.8$ contours to distribute high above the endwall. No coolant stream is apparent as $\theta \approx 0.9$ on the fillet surface at $Z/P < 0.10$ for the fillet-1 in Fig. 5. Note, the concentration of the coolant streams of $\theta < 0.7$ near the pressure side (PS) at $Z/P > -0.15$ in plane-1 of Fig. 4 for all the cases. The low values of θ on the endwall near the PS is significant as the coolant coverage on the pressure-side endwall according to [27, 35, 36] is difficult to provide with the high turning away of the endwall flows from the pressure side. For the fillet-1 in Figs. 4 and 5, the color level above the $\theta = 0.8$ contour line has lower values than the other cases, but the θ values in this region are about 0.90 for all the cases. The values of θ increase in planes-1 and 2 as the M_{in} decreases with the coolant mass flux and momentum.

Figures 6 and 7 show the θ distributions for $M_{in} = 1.4$ and 2.2, respectively, in plane-3 where the pressure side-leg and suction side-leg vortices combine to form the single passage vortex near the suction side. The plane location between the pressure-side and suction-side in the three-dimensional passage and the film-cooling configurations are shown at the bottom of the plot area in Fig. 6. Note that the endwall boundary layer separation region is located upstream of the plane-3 according to [35-38]. The concentrations of $\theta \leq 0.8$ contours and regions along the pitchline Z/P for all the cases are due to the coolant distributions. This signifies that the coolant from the upstream slots can effectively slip under the strong separation region and provide coverage downstream of the boundary layer separation region. Because of the high turning of streamlines [23, 36] and yaw angles (shown later in Fig. 14) toward the suction side in endwall region, the coolant streams also turn toward the suction side and low values of θ concentrate at the suction side of plane-3 for the baseline-1 in Figs. 6 and 7. However, the absence of any $\theta \leq 0.8$ contours near the suction side (SS) for the baseline-2 and fillet-1 in Figs. 6 and 7 indicates no effective coolant streams due to the mixing and lifting-off by the passage vortex. The decrease of θ values at different locations and shift of low values of $\theta \leq 0.7$ toward the pressure side (PS) are noticeable from Fig. 6 to Fig. 7 as the M_{in} increases for the different cases. The local film-cooling effectiveness can be predicted to be high at the concentrated θ of low values and thus depends upon the blowing ratio and

coolant mass flux. The results of [27, 35, 37-39] show the pressure side (PS) region downstream of the endwall boundary layer separation is difficult to reach for the upstream film-cooling flow. The low values of θ near the PS in Fig. 7 are thus very desirable for the effective full-coverage of the film-cooling on endwall. However, the low values of θ at $Y/S > 0.03$ in both Figs. 6 and 7 are caused most likely by the coolant jet lift-off and penetration into the boundary layer which are very prominent for all the cases in Fig. 7. The lift-off coolant into the boundary layer has little effects on the film-cooling effectiveness on endwall. The passage vortex structures along their travel paths interact with the coolant streams and significantly affect the θ distributions. The effects of the passage vortex legs are discussed later in Figs. 9 to 12.

The local pitchwise θ values along the Z/P at a constant Y/S location in plane-3 are arithmetically averaged. The average θ values are plotted against the Y/S locations in Fig. 8 for M_{in} = 1.0 to 2.2. As expected, the average θ values increase along Y/S away from the endwall because of the mixing of coolant with endwall flows and absence of coolant streams higher above the endwall. The average θ values in the region of $Y/S < 0.1$, which is the inlet boundary layer thickness, are important for the film-cooling effectiveness and always lower for the baseline-1, baseline-2, and fillet-2 than for the fillet-1 at any M_{in}. Closer to the endwall at $Y/S < 0.05$ the average θ values are the lowest for the fillet-2 case.

The distributions of normalized vorticity, $\omega_x C/U$ are shown in Figs. 9 to 12 near the endwall region in planes-2 and 3. The blue triangular regions at the bottom corners of the planes represent the filleted regions. The vorticity, ω_x is perpendicular to the respective plane and is determined from the local velocity components (v, w) after fitting the spline curves on the velocity distributions and obtaining derivatives along the spline fits numerically. In the figures, the negative values of $\omega_x C/U$ are represented by the broken contour lines while the positive $\omega_x C/U$ are represented by the solid contour lines. The pressure and suction sides (PS and SS) of the passage are indicated at the side-edges of the respective plots. The contour-levels used in Figs. 9 to 12 are shown at the bottom of the plots in the respective figure.

Figure 9 presents the $\omega_x C/U$ contours in plane-2 for M_{in} = 1.4 and 2.2 and compares the cases between baseline-2 and fillet-2. The plane-2 location and film-cooling slot configurations in the passage are also included in the figure. The large negative contour region of $\omega_x C/U$ near SS for the baseline-2 in Figs. 9(a) and 9(c) is caused by the suction side-leg of passage vortex as it interacts with the film-cooling flow. For fillet-2, in comparison, near the SS at the corresponding blowing ratio the negative $\omega_x C/U$ region is smaller due to the weaker suction side-leg vortex. In general for both baseline-2 and filet-2, the negative $\omega_x C/U$ lines just above the endwall along the Z/P locations away from the SS are caused by the film-cooling flow only, while the positive $\omega_x C/U$ lines all along the Z/P locations are caused by the

interactions of the film-cooling flow with the boundary layer [23]. With the blowing ratio (M_{in}) from 1.4 to 2.2, the film-cooling mass flux, jet momentum, interactions between the coolant jet and endwall flows, and the resulting $\omega_x C/U$ contour regions of both positive and negative everywhere also increase in Fig. 9. When compared between the baseline-2 and fillet-2, both the negative and positive vorticity regions at $Z/P > 0.05$ are larger for the fillet-2 away from the SS. The weaker suction side-leg vortex and better coolant distributions along endwall for the fillet-2 are responsible for the differences between the cases in Fig. 9 which could not be inferred from the results of Fig. 5. The fillet redistributes the boundary layer flows, changes vortex axis, and weakens the pitchwise pressure gradient along with the passage vortex legs as shown in [2, 4-6] improving the coolant distributions and reducing interactions between the coolant streams and boundary layer. Note that the influences of the slot film-cooling jet on the passage vortex structures are detailed in [23] in the present cascade and hence, are not discussed here for brevity.

Figure 10 compares the $\omega_x C/U$ for the film-cooling cases between baseline-1 and fillet-1 for the blowing ratio of 2.2 in plane-2. With all the slots open, the coolant jet mass flux and momentum are high enough in baseline-1 to cause the negative $\omega_x C/U$ contours almost everywhere along the Z/P locations. The distributions of negative and positive $\omega_x C/U$ at $Z/P < 0.1$ for the baseline-1 are the results of coolant flow interacting with the suction-side leg vortex and boundary layer. In comparisons to the baseline-1 in Fig. 10, the fillet-1 configuration provides similar $\omega_x C/U$ distributions in the $Z/P > 0.1$ region because of the similar coolant distributions (refer to Fig. 5) and effects. However, the negative $\omega_x C/U$ distributions for the fillet-1 in the $Z/P < 0.1$ region are primarily the results of the suction side-leg vortex with little influences from the coolant jets as the leading-edge slot is fully closed. The temperature distributions of Fig. 5 earlier show the slot openings and fillet geometry change the distributions of mass flux, trajectories, and momentums of the coolant streams. The comparisons of the results between Fig. 9(c, d) and Fig. 10 for $M_{in} = 2.2$ show the region of negative $\omega_x C/U$ at $Z/P > 0.1$ are larger for the baseline-1 and fillet-1. However, the coolant stream concentration is high at $Z/P > 0.1$ for all the film-cooling configurations as shown in Fig. 5. Note that the vortex motion lifts up the coolant streams from the endwall when the passage-vortex legs and film-cooling flow interact [27, 35]. Clearly, the suction side-leg vortex with the smaller region of negative $\omega_x C/U$ near SS is weaker for the baseline-1 in Fig. 10 than for the baseline-2 in Fig. 9(c) and for the fillet-2 in Fig. 9(d) than for the fillet-1 in Fig. 10. The larger and stronger structure of the suction side-leg vortex with high vorticities for the baseline-2 and fillet-1 cases will then reduce the local coverage and effectiveness of the film-cooling.

Figure 11 compares the $\omega_x C/U$ distributions between the film-cooling configurations of baselines and fillet-2 for $M_{in} = 1.4$ and 2.2 in plane-3. The passage vortex legs (both pressure side-leg and suction side-leg) in the plane-3 location advect at the suction side (SS) as indicated in [23, 36]. The results of Figs. 6

and 7 in plane-3 earlier show the coolant streams turn and concentrate toward the suction side. The positive and negative $\omega_x C/U$ contours between SS and Z/P = 0.15 in Fig. 11 indicate the passage vortex legs as they interact with the coolant flows. Because of the high coolant concentration and interactions of the coolant streams with the passage vortex legs, the $\omega_x C/U$ contours near SS in Fig. 11 cannot clearly identify the strength and size of the vortex legs alone for all the cases. The vorticities away from the SS at Z/P > 0.15 along the pitchline are then caused by the coolant flows (negative vorticities) and interactions between the coolant and boundary layer (positive vorticities). More regions of high magnitude $\omega_x C/U$ appear along Z/P in Fig. 11 for each configuration as the coolant mass flux, momentum, and distributions increase when M_{in} increases from 1.4 to 2.2. The high magnitude $\omega_x C/U$ contours for the M_{in} = 2.2 cases in Figs. 11(d-f) away from the endwall at Y/S > 0.03 are the effects of the coolant jet penetration in the boundary layer (refer to Figs. 6 and 7) which are more prominent for the baseline-2 than for the others. Comparisons among Figs. 11(a), 11(b), and 11(c) for M_{in} = 1.4 show the vorticities just above the endwall apparently cover the entire Z/P pitch-length better for the fillet-2 as a result of the better coolant coverage than for the baseline configurations. However, in the Figs. 11(d, e, f) for M_{in} = 2.2, the vorticity distributions on endwall along the Z/P pitch-length are better for the baseline-2 configuration than for the others. Relating the θ data of Figs. 6 and 7 with the $\omega_x C/U$ data of Fig. 11 it can be concluded that the coolant coverage on endwall at plane-3 for a blowing ratio is primarily dependent upon the mass flux, momentum, and trajectory of the coolant as well as the lift-off of the coolant by the passage vortex separation region located upstream. The low values of air temperature simply reveals the presence of coolant streams, but do not properly illustrate the amount of coolant mass flux and momentum. The interactions between the coolant streams and boundary layer also cause the streams to lose mass and momentum and consequently, loss of coverage and effectiveness on the endwall.

The $\omega_x C/U$ distributions for the fillet-1 configuration of film-cooling in plane-3 for M_{in} = 1.4 and 2.2 are presented in Fig. 12. As expected, the $\omega_x C/U$ distributions along the Z/P locations on endwall are larger in magnitudes and regions as the M_{in} increases. In accordance with Fig. 7, the results of $\omega_x C/U$ in Fig. 12 then confirm the coolant coverage on endwall is better at the higher M_{in}. When the fillet-1 in Fig. 12 is compared with the other configurations in Fig. 11 for both M_{in} = 1.4 and 2.2, the coolant coverage on endwall for the fillet-1 seems better on the pressure side region (Z/P > 0.25) as all the slots are open. The suction-side leg vortex represented by the negative $\omega_x C/U$ contours near SS is not clearly apparent in Fig. 12 as the vortex has weakened substantially.

Figures 13 and 14 present the yaw angle deviations, ΔYaw of the flow in plane-2 and plane-3, respectively, for the baseline and fillet configurations of film-cooling for the blowing ratio, M_{in} = 2.2. The filleted area is indicated by the shaded triangular region. The measured yaw angle at the mid-span

height (Y/S =0.5) in a given Z/P location is subtracted from the local yaw angle at the same Z/P location to determine the yaw angle deviation, ΔYaw. The "+ve" and "-ve" senses of yaw angle are indicated in Fig. 1(b). The broken contour lines of Figs. 13 and 14 represent the negative ("-ve") ΔYaw. The results of ΔYaw distributions near the endwall in Figs. 13 and 14 are caused by the film-cooling flow and interactions of the coolant streams with the boundary layer and passage vortex legs. The results in [5] indicate that the fillet without the film-cooling and in [23] indicate that the slot film-cooling without the filet reduce the ΔYaw in the endwall region. The reduction of the pitchwise pressure gradient due to the fillet and the higher kinetic energy of the coolant streams adding momentum in the boundary layer mixing reduce the streamline turning toward the suction side. Without the film-cooling and fillet, the ΔYaw values near the endwall are generally "+ve" with high magnitudes because of the high turnings of the streamlines toward the suction side [2, 36]. With the film-cooling the low magnitudes of ΔYaw are desirable near the endwall for the uniform coolant distributions along the pitchline. The coolant streams are less likely to amass toward the suction side when the streamline turnings near the endwall are reduced. The low values of ΔYaw distributions also weaken the passage vortex [4, 5] and may benefit the film-cooling of discrete holes inside the blade passage.

In the plane-2 of Fig. 13, the ΔYaw values are generally "+ve" because of the streamline turning near the endwall. The ΔYaw distributions specially in the $Y/S < 0.10$ locations for all the configurations are different from each other. However, the ΔYaw distributions in the small region covered by $Z/P > 0.12$ and $Y/S < 0.05$ are very alike, which are also evidenced in the θ distributions previously, due to the coolant jets from the 55 mm slots. Near the SS corner in $Z/P < 0.10$ locations, the ΔYaw values for the baseline-1 are different from the baseline-2 as the suction side-leg vortex is stronger for the baseline-2 (refer to Figs. 9 and 10). When the fillets are employed in Figs. 13(c, d), the ΔYaw values near the SS corner in $Z/P < 0.10$ change substantially as the suction side-leg vortex weakens for the fillet-1 compared to the baseline-1 and for the fillet-2 compared to the baseline-2. The coolant-stream temperature and vorticity near the SS corner for the fillets shown previously cause the differences of ΔYaw near the SS between the fillet-1 and fillet-2.

The fillets in Figs. 14(c, d) have changed the near endwall ΔYaw distributions of the baselines in Figs. 14(a, b) when the data in plane-3 are presented in Fig. 14 for the same blowing ratio. The "-ve" values of ΔYaw just above the endwall and along almost the entire pitchline Z/P for all the configurations but for the fillet-1 are the evidences of coolant streams in spite of the influences of the boundary layer separation upstream and the passage-vortex located near SS. The θ distributions in Fig. 7 previously provide the coolant stream distributions along the pitchline in plane-3 and also show some lack in the

coolant concentrations. With the fillet-1 the "-ve" ΔYaw in Fig. 14(c) are confined only in the mid-pitch region of $0.20 < Z/P < 0.50$. Note the concentration of the "-ve" ΔYaw contours adjacent to endwall in $0.20 < Z/P < 0.40$ because of the coolant stream concentration. The data distributions adjacent to the endwall in Fig. 14 are thus very conducive for the coolant presence everywhere along the pitchline for the baseline and fillet-2 configurations. In comparisons, the ΔYaw distributions for the fillet-1 in Fig. 14(c) are only conducive for the coolant distributions in the mid-pitch locations away from the SS and PS. The "-ve" ΔYaw values high above the endwall at $Y/S > 0.1$ in Fig. 14 for the baseline and fillet-2 cases are most likely caused by the coolant lift-off and mixing of some coolant streams with the boundary layer at the high blowing ratio. As the coolant stream momentum decreases along with the M_{in}, the magnitudes of "+ve" ΔYaw increase and "-ve" ΔYaw decrease in planes-2 and 3.

The effects of the film-cooling and fillet on the passage vortex are manifested in the total-pressure loss across the vane cascade. Figure 15 presents the distributions of the total-pressure loss coefficients, $C_{pt,loss}$ in plane-4 for the four cases of film-cooling for $M_{in} = 2.2$. Plane-4 is located just downstream of the passage exit. The relative positions of the vane trailing-edge (TE) and plane-4 are shown in the three-dimensional passage at the bottom of the plots in Fig. 15. The blocked slots i.e, partially darkened slots upstream of the vane leading-edge in the image of baseline-2 configuration are fully open for the baseline-1 configuration. The location of vane trailing-edge upstream of the plane-4 is indicated at $Z/P = 0.2$ in the plots of Fig. 15. The local $C_{pt,loss}$ values of the figure are estimated in Eq. (4) from the measured total pressure, P_t in plane-4. The local total pressure losses, $(P_{t,r} - P_t)$ are high in the passage vortex and TE wake regions resulting in the high values of $C_{pt,loss} > 1.0$ between $0.22 < Z/P < 0.4$ and $0.15 < Z/P < 0.22$, respectively. The passage vortex-core is then located between $0.15 < Y/S < 0.3$ and $0.12 < Y/S < 0.25$ for the baseline-1 and fillet-1, respectively, in Fig. 15. However, the same is located between $0 < Y/S < 0.12$ much nearer to the endwall for the baseline-2 and fillet-2. Note the high $C_{pt,loss}$ contours in small region above the endwall in $Y/S < 0.15$ and between of $0.22 < Z/P < 0.4$ for the baseline-1 and fillet-1 are also caused by the passage vortex and its interactions with the coolant streams and boundary layer. The passage vortex structure is thus larger for the baseline-1 and fillet-1 than for the other two configurations. However, the results of baseline-1 in the upstream planes previously show otherwise where the suction side-leg vortex seems weaker. The losses due to the mixing of coolant with the passage vortex structures along the vane passage must have contributed to the larger passage vortex for the baseline-1 in plane-4. The high values of $C_{pt,loss} > 1.0$ in other locations just above the endwall of Fig. 15 are caused by the pressure losses in the boundary layer and mixing losses of the coolant interacting with the boundary layer. The region of mixing losses at the endwall is very comparable among

the four cases. The full structure of the passage vortex is not apparent in Fig. 15 for any case of the film-cooling as part of it is succumbed into TE wake in plane-4. The outer region and core region of the passage vortex outside the TE wake show about the same $C_{pt,loss}$ distributions for all the cases. However, the $C_{pt,loss}$ distributions confirm that the passage vortex location is influenced by the film-cooling and fillet configurations as the coolant mass-flux and momentum energize the boundary layer. The present $C_{pt,loss}$ distributions for the baseline film-cooling configurations are higher specially in the passage vortex and trailing edge regions compared to those in [23, 28] as the plane-4 is located about 7 mm upstream of the exit plane of [23, 28]. The distributions of loss coefficient between $0.5 < C_{pt,loss} < 1.0$ outside the boundary layer and TE wake regions change little between the present investigations and [23, 28], but the losses in the passage vortex and wakes dissipate downstream.

$$\mathrm{C_{pt,loss}} = \frac{\left(\mathrm{P_{t,r}} - \mathrm{P_t}\right)}{\left(\mathrm{P_{t,r}} - \mathrm{P_{s,r}}\right)} \tag{4}$$

The influences of the blowing ratio, M_{in} and fillet on the overall pressure losses in plane-4 are shown by the mass-averaged loss coefficient, $(C_{pt,loss})_{Mass\text{-}av}$ and the ratio $(C_{pt,loss})_{Mass\text{-}av}$/MFR distributions in Fig. 16. The mass-averaged coefficient, $(C_{pt,loss})_{Mass\text{-}av}$ is determined from the numerical integration of the right hand side of Eq. (5) where $(P_{t,r} - P_t)$ is the distribution of local pressure losses in plane-4. The area of integration, A in the equation covers the measurement area in plane-4 and dA is determined based on the spatial resolutions of the data locations. The mass fraction ratios (MFR) in Fig. 16(b) are obtained from Table 4. The mass fraction is the ratio of coolant flow rate (M_c) from the four or two slots to air-flow rate (M_a) in a vane passage based on the freestream reference velocity (U). The coolant flow rate is measured at the orifice meter in the coolant supply circuit. Note that ($0.5M_a$) in Eq. (5) indicates the mass-flow rate in the measurement region between $0 \leq Y/S \leq 0.5$. The $(C_{pt,loss})_{Mass\text{-}av}$ in Eq. (5) thus includes the coolant mass and is also referred to as the overall mixed-out losses. The higher the $(C_{pt,loss})_{Mass\text{-}av}$, the higher the total pressure losses across the cascade passage.

$$\left(\mathrm{C_{pt,loss}}\right)_{\mathrm{Mass-av}} = \int_A \frac{\rho_r u\left(\mathrm{P_{t,r}} - \mathrm{P_t}\right)}{\left(\mathrm{P_{t,r}} - \mathrm{P_{s,r}}\right)(0.5M_a)}\,\mathrm{dA} \tag{5}$$

The mass-averaged $(C_{pt,loss})_{Mass\text{-}av}$ in Fig. 16(a) for all the four cases are compared as the M_{in} varies. In general, the $(C_{pt,loss})_{Mass\text{-}av}$ distributions increase slightly from $M_{in} = 1.0$ to either $M_{in} = 1.4$ or 2.2 and then decrease slightly as the M_{in} increases further for all the cases. The distribution of $(C_{pt,loss})_{Mass\text{-}av}$ is the highest between $1.0 \leq M_{in} \leq 1.8$ for the baseline-2 case and at $M_{in} > 1.8$ for the baseline-1 case. The average loss coefficients in Fig. 16(a) are generally about the same and smaller for the fillet cases at all

the M_{in} values. For the baseline-1, the average loss coefficients are also the same as the fillet cases when $M_{in} \leq 1.4$. As the total pressure losses in the regions of passage vortex, TE wake, and freestream flow are about the same among the different cases, the mixing losses near the endwall region contribute to the high values of $(C_{pt,loss})_{Mass\text{-}av}$. The higher momentums of the coolant stream at higher blowing ratios decrease the total pressure deficits, $(P_{t,r} - P_t)$ near the endwall to reduce the $(C_{pt,loss})_{Mass\text{-}av}$. As shown in Fig. 16(a), the maximum decrease in the $(C_{pt,loss})_{Mass\text{-}av}$ of the baseline-1 cooling configuration is by about 11% when the fillet-1 is employed. The maximum decrease in the $(C_{pt,loss})_{Mass\text{-}av}$ of the baseline-2 cooling configuration is by about 8% when the fillet-2 is employed. Thus, the fillet-1 is more effective in reducing the $(C_{pt,loss})_{Mass\text{-}av}$ of the baseline-1 when $1.8 \leq M_{in} \leq 2.8$. On the contrary, the fillet-2 is more effective in reducing the $(C_{pt,loss})_{Mass\text{-}av}$ of the baseline-2 when $1.0 \leq M_{in} \leq 1.8$. The mass-averaged $(C_{pt,loss})_{Mass\text{-}av}$ distributions in Mahmood and Arnachellan [23] are generally about 50% less of the present values of Fig. 16(a) as the plane-4 of the present measurements is located closer to the passage actual exit.

The ratios $(C_{pt,loss})_{Mass\text{-}av}$/MFR of Fig. 16(b) signify the mass-averaged pressure loss coefficients per unit mass fraction of the coolant delivered for all the film-cooling configurations. As shown, the ratios $(C_{pt,loss})_{Mass\text{-}av}$/MFR are about the same at all M_{in} and decrease as the M_{in} increases. The decrease of the ratio in Fig. 16(b) is significant only at $M_{in} < 1.8$. At the higher M_{in}, the pressure loss coefficient decreases, but the higher amount of coolant flow outweighs the benefit of pressure loss reduction. As the M_{in} increases, both the coolant mass flux and work load on the turbine-compressor to deliver the required coolant flow increase. The data in Fig. 16 thus suggest that the present film-cooling configurations can provide only limited benefits on the pressure loss reduction across the vane passage at very high bleed flow rate, but at the expense of thermal efficiency of the gas turbine.

4. Conclusions

Experimental results of the flow temperatures, axial vorticities, flow deviation angles, and total pressure loss coefficients near the endwall are presented in a passage of a linear vane-cascade with the endwall fillets and film-cooling flow from the bleed slots at the passage inlet. The results show the coolant stream distributions with and without the fillet. The effects of the fillet on the interactions between the film-cooling flow and endwall flow and on the overall pressure losses across the cascade are illustrated. The vane-cascade is housed in an atmospheric wind tunnel. Two different large fillets around the vane profile and endwall junction are employed covering the bleed slots partially. Fillet-2 is slightly smaller than fillet-1. The bleed slot-flow without the fillet is referred to as the baseline configuration for comparisons. The slots are fully open in the baseline-1 configuration and are partially closed at the vane leading-edge in the baseline-2 configuration. The inlet Reynolds number for the main flow is 2.0E+05.

The inlet blowing ratio for the film-cooling flow varies from 1.0 to 2.8 with the temperature and density ratios of coolant to main flow both at about 1.0. The objectives are to investigate if the fillets benefit the film-cooling distributions and reduce the secondary pressure losses in the cascade.

The temperature-fields show the distributions of coolant streams on endwall both upstream and downstream of the endwall boundary layer separation region. The presence of coolant on the passage pressure side particularly in the downstream of the separation region for all four film-cooling configurations is notable. However, the pitchwise concentrations and distributions of the coolant streams on the endwall are usually lower for the fillet-1 configuration than for the other configurations. The film-cooling configuration of fillet-2 outperforms the other configurations in maintaining the high coolant concentrations on endwall irrespective of the blowing ratio employed. The best film-cooling effectiveness on endwall may then be obtained with the fillet-2.

The results of vorticity and flow yaw angles indicate that the fillets primarily affect the passage vortex and the boundary layer flow by reducing the suction side-leg vortex and yaw angle deviations from the mid-span flow. When the fillets are employed in the baseline cooling configurations, the vorticities and yaw angle deviations are reduced. The fillet-2 performs better than the fillet-1 to reduce the yaw angle deviations. The yaw angle deviations and coolant distributions are important as they affect the secondary pressure losses and film-cooling effectiveness on the endwall. The local secondary or total-pressure losses at the passage exit, due to the mixing of coolant streams with the boundary layer, trailing edge wake flow, and passage vortex, are reduced when the fillets are employed. Consequently, the overall (mass-averaged) total-pressure losses at the passage exit are always smaller for the fillet cases than for the baseline cases of film-cooling configuration at all the blowing ratios. The overall losses are then the lowest for the fillet-1. The results also reveal the overall pressure losses decrease at very high blowing ratios when the coolant mass flux and momentum are higher energizing the boundary flow. Thus, the fillet-1 is the best in the overall total pressure reduction and the fillet-2 is the best in the coolant flow distributions on endwall among all four film-cooling configurations.

The amount of coolant mass flux is very high at the higher blowing ratios for all four film-cooling configurations. The quantity of $(C_{pt,loss})_{Mass\text{-}av}$/MFR signifying the overall total-pressure loss coefficient per unit coolant mass flux ratio is then surprisingly about the same with and without the fillets and decreases as the mass flux ratio increases. The requirements of large coolant flow rate thus outweigh the benefits of lowering the overall total-pressure losses for all the film-cooling configurations. The results of the present investigation are beneficial for the endwall film-cooling design and optimization in the gas turbine passages. Measurements of the endwall film-cooling effectiveness for the four configurations can be potentials for further research.

Acknowledgements

The financial supports of the National Research Foundation and Armaments Corporation program of the South African government are gratefully acknowledged. Barbara Huyssen's help for the filet-2 design is also acknowledged.

Nomenclature

C, C_{ax} =	Vane profile actual and axial chord
$C_{Ps,endwall}$, $C_{Pt,loss}$ =	Pressure coefficient: endwall and total loss
L, W =	Film-cooling slot geometry
M_{in}, (MFR) =	Inlet blowing ratio (BR) and mass fraction of coolant
M_a =	Passage mass flow rate
P, S =	2-dimensional vane pitch and span
PS, SS =	Passage pressure and suction side
$P_{s,b}$ =	Local pressure on vane profile
$P_{s,r}$, $P_{t,r}$ =	Reference pressure: static and total
$P_{t,b}$ =	Total pressure inside plenum box
Re =	Inlet Reynolds number to cascade
T_a, T_r =	Air temperature (K) in passage and reference
$T_{c,b}$, $\rho_{c,b}$ =	Air temperature (K) and density in coolant plenum
U, u =	Axial velocity: Reference, local
X, Y, Z =	Local coordinates
X_G, Y_G, Z_G =	Global coordinates
s =	Distance along vane profile
v, w =	Velocity components along (Y, Z)
μ, ρ_r =	Air density and viscosity in reference plane
ω_x =	Axial vorticity
θ =	Non-dimensional temperature
"+ve", "-ve" =	Positive and negative quantities

References

[1] P. Ligrani, G. Potts, A. Fatemi, A., Endwall aerodynamic losses from turbine components within gas turbine engines, Propulsion and Power Research, published online 23-Jan. (2017), http://dx.doi.org/10.1016/j.jppr.2017.01.006 [retrieved 16-Feb 2017].

[2] M.B. Kang, K. Thole, Flow field measurement in the endwall region of a stator vane, J. Turbomach. 122 (3) (2000) 458-466.

[3] K. Harmanson, S. Kern, G. Picker, S. Parneix, Predictions of external heat transfer for turbine vanes and blades with secondary flowfields, J. Turbomach. 125 (1) (2003) 107-113.

[4] G.I. Mahmood, R. Gustafson, S. Acharya, Experimental investigation of flow structure and nusselt number in a low-speed linear blade passage with and without leading-edge fillets, J. Heat Trans., 127 **(**2005) 499-512.

[5] G.I. Mahmood, S. Acharya, Experimental investigation of secondary flow structure in a blade passage with and without leading edge fillets, J. Fluids Eng., 129 **(**2007) 253-262.

[6] G.A. Zess, K. Thole, Computational design and experimental evaluation of using a leading edge fillet on a gas turbine vane, J. Turbomach. 124 (2) (2002) 167-175.

[7] M.W. Benner, S.A. Sjolander, S.H. Moustapha, The influence of leading edge geometry on secondary losses in a turbine cascade at the design incidence, J. Turbomach. 126 (2) (2004), 277-287.

[8] S. Becz, M.S. Majewski, L.S. Langston, An experimental investigation of contoured leading edges for secondary flow loss reduction, Proc. ASME Turbo Expo, Paper No. GT-2004-53964 (2004) 1407-1415.

[9] Z.-J. Wei, W.-Y. Qiao, J. Liu, W.-H. Duan, W.-H., Reduction of endwall secondary flow losses with leading-edge fillet in a highly loaded low-pressure turbine, Proc. Institute of Mechanical Engineers, Part A: J.of Power and Energy 230 (2) (2016**)** 184-195.

[10] A.T. Lethander, K.A., Thole, G., Zess, J. Wagner, Vane-endwall junction optimization to reduce turbine vane passage adiabatic wall temperatures, J. Propulsion and Power 20 (6) (2004) 1096-1104.

[11] S. Mank, L. Duerrwaechter, M. Hilfer, R. Williams, S. Hogg, G. Ingram, Secondary flows and fillet radii in a linear turbine cascade, Proc. ASME Turbo Expo, Paper No. GT-2014-25458 (2014).

[12] Y. Shi, J. Li, Z. Feng, Influence of rotor blade fillets on aerodynamic performance of turbine stage, Proc. ASME Turbo Expo, Paper No. GT-2010-23721 (2010) 1657-1668.

[13] M. Thomas, T. Povey, Improving turbine endwall cooling uniformity by controlling near-wall secondary flows, J. Aerospace Engineering 0 (0) (2016) 1-17.

[14] S. Salvadori, L. Ottanelli, M. Jonsson, P. Ott, F. Martelli, Investigation of high-pressure turbine endwall film-cooling performance under realistic inlet conditions, J. Propulsion and Power 28 (4) (2012) 799-810.

[15] E.de la R. Blanco, H.P. Hodson, R. Vazquez, Effect of leakage flows and the upstream platform geometry on the endwall flows of a turbine cascade, J. Turbomach. 131 (1) (2009) 0110041-0110049.

[16] M. Papa, V. Srinivasan, R.J. Goldstein, F. Gori, Effect of gap geometry on the cooling effectiveness of the wheelspace coolant injection upstream of a row of rotor, Heat Transfer Research 41(6) (2010) 651-667.

[17] G. Barigozzi, G. Franchini, A. Perdichizzi, M. Maritano, R. Abram, Purge flow and interface gap geometry influence on the aero-thermal performance of a rotor blade cascade, Int. J. Heat and Fluid Flow 44 **(**2013) 563-575.

[18] W –G. Wan Aizon, K -i Funazaki, T. Miura, Purge flow effect on aerodynamics performance in high-pressure turbine cascade, J. Mechanical Science and Technology 27 (6) (2013) 1611-1617.

[19] G. Barigozzi, H. Abdeh, A. Perdichizzi, M. Henze, J. Krueckels, Aerothermal performance of a nozzle vane cascade with a generic nonuniform inlet flow condition - Part II: influence of purge and film cooling injection, J. Turbomach. 139 (2017) 1010041-1010049.

[20] C. McLean, C. Camci, B. Glezer, Mainstream aerodynamic effects due to wheelspace coolant injection in a high-pressure turbine stage: Part I - aerodynamic measurements in the stationary frame, J. Turbomach. 123 (2001) 687-696.

[21] K. Du, J. Li, Numerical study on the effects of slot injection configuration and endwall alignment mode on the film cooling performance of vane endwall, Int. J. Heat and Mass Transfer 98 (2016) 768-777.

[22] A.A. Thrift, K.A. Thole, K.A., Influence of flow injection angle on a leading-edge horseshoe vortex, Int. J. Heat and Mass Transfer 55 (2012) 4651-4664.

[23] G.I. Mahmood, K. Arnachellan, Effects of upstream endwall film-cooling on a vane cascade flow-field, J. Propulsion and Power 34 (2) (2018) 460-468.

[24] R.A. Oke, T.W. Simon, Film cooling experiments with flow introduced upstream of a first Stage nozzle guide vane through slots of various geometries, Proc. ASME Turbo Expo, Paper No. GT2002-30169 (2002).

[25] F. Ornano, T. Povey, Experimental and computational study of the effect of momentum-flux ratio on high-pressure nozzle guide vane endwall cooling systems, J. Turbomach. 139 (2017) 1210021-12100214.

[26] G. Barigozzi, A. Perdichizzi, R. Abram, Improving the film cooling of a rotor blade platform, ASME J. Fluids Eng. 140 (2018) 0211011-0211016.

[27] Y. Zhang, X. Yuan, P. Ligrani, Film cooling effectiveness distribution on first-stage vane endwall with and without leading-edge fillets, Int. J. Heat and Mass Transfer 66 (2013) 642-645.

[28] G.I. Mahmood, K. Arnachellan, Flow-field in a linear vane cascade with endwall fillet and film-cooling, Published by ASME, Proc. ASME 2018 5th Joint US-European Fluids Engr Summer Conf., ASME Paper No. FEDSM2018-83140 (2018) V002T11A004.

[29] K. Arnachellan, Aerodynamic Loss Reduction in a Vane Cascade with Leading Edge Fillet and Upstream Endwall Film Cooling, MEng. Thesis, Mech. and Aero. Engineering, University of Pretoria, South Africa, 2017.

[30] L.P. Timko, Energy Efficient Engine High Pressure Turbine Component Test Performance Report, Contract Report for NASA, Report No. NASA CR-168289, 1990.

[31] K.A. Thole, D.G. Knost, Heat transfer and film cooling for the endwall of a first stage turbine vane, Int. J. Heat Mass Transfer 48 (2005) 5255–5269.

[32] G. Barigozzi, G. Franchini, A. Perdichizzi, M. Maritano, R. Abram, Influence of purge flow injection angle on the aerothermal performance of a rotor blade cascade, J. Turbomach. 136 (2014) 0410121-0410129.

[33] R.J. Moffat, Describing the Uncertainties in Experimental Results, Exp. Thermal and Fluid Sciences 1 (1) (1988) 3-17.

[34] T.G. Beckwith, R.D. Marangoni, J.H. Lienhard, Mechanical Measurements, sixth ed., Pearson Prentice Hall, New Jersey, 2007, pp. 42-45, 54-59.

[35] S. Friedrichs, H.P. Hodson, and W.N. Dawes, Distribution of film-cooling effectiveness on a turbine endwall measured using the Ammonia and Diazo technique, J. Turbomach. 118 (1996) 613-621.

[36] S. Acharya, G.I. Mahmood, Turbine Blade Aerodynamics, in: Gas Turbine Handbook, NETL of the US Department of Energy, Ch. 4.3, 2007, pp. 363-388.

[37] L. Song, P. Zhu, J. Li, Z. Feng, Effect of purge flow on endwall flow and heat transfer characteristics of a gas turbine blade, Applied Thermal Eng. 110 (2017) 504-520.

[38] A.F. Chen, C –C. Shiau, J –C. Han, Turbine blade platform film cooling with fan-shaped holes under simulated swirl purge flow and slashface leakage conditions, J. Turbomach. 140 (2017) 0110061-01100611.

[39] S –J. Li, J. Lee, J –C. Han, L. Zhang, H –K. Moon, Influence of mainstream turbulence on turbine blade platform cooling from simulated swirl purge flow, Applied Thermal Eng. 101 (2016) 678-685.

Table 1

Geometric parameters of vane cascade

C_{ax} (m)	C (m)	C/S	C/P	Incidence
0.203	0.355	1.479	1.328	0°

Table 2

Slot opening for film-cooling flow

Baseline-1 (no fillet)	Baseline-2 (no fillet)	Fillet-1	Fillet-2
55 mm slot open, 82 mm slot open	55 mm slot open, 82 mm slot 24% open	55 mm slot open, 82 mm slot closed	55 mm slot open, 82 mm slot 24% open

Table 3

Reference flow-parameters ($2.5C_{ax}$ upstream of cascade)

Freestream velocity, U	10.0 m/s
$P_{s,r}$ ("-ve" gage)	60 kPa
Boundary layer thickness, δ/S	10%
Streamwise turbulence intensity	3%
Temperature (T_r), density (ρ_r)	298 K, 1.02 kg/m^3
Coolant to reference: ($\rho_{c,b}/\rho_r$)	1.0
Coolant to reference: ($T_{c,b}/T_r$)	1.0-0.94
Reynolds number, Re = ($\rho_r UC/\mu$)	2.0E+05
Inlet Mach number, ($U/(\gamma RT_r)^{0.5}$)	0.03

Table 4

Mass fraction ratio (M_c/M_a) of coolant flow to passage flow

BR =	1.0	1.4	1.8	2.2	2.8
Baseline-1	0.00580	0.02661	0.0656	0.08110	0.11182
Baseline-2	0.00576	0.02272	0.04460	0.06022	0.09480
Fillet-1	0.00523	0.01711	0.04397	0.06020	0.09409
Fillet-2	0.00576	0.02290	0.05920	0.07350	0.09430

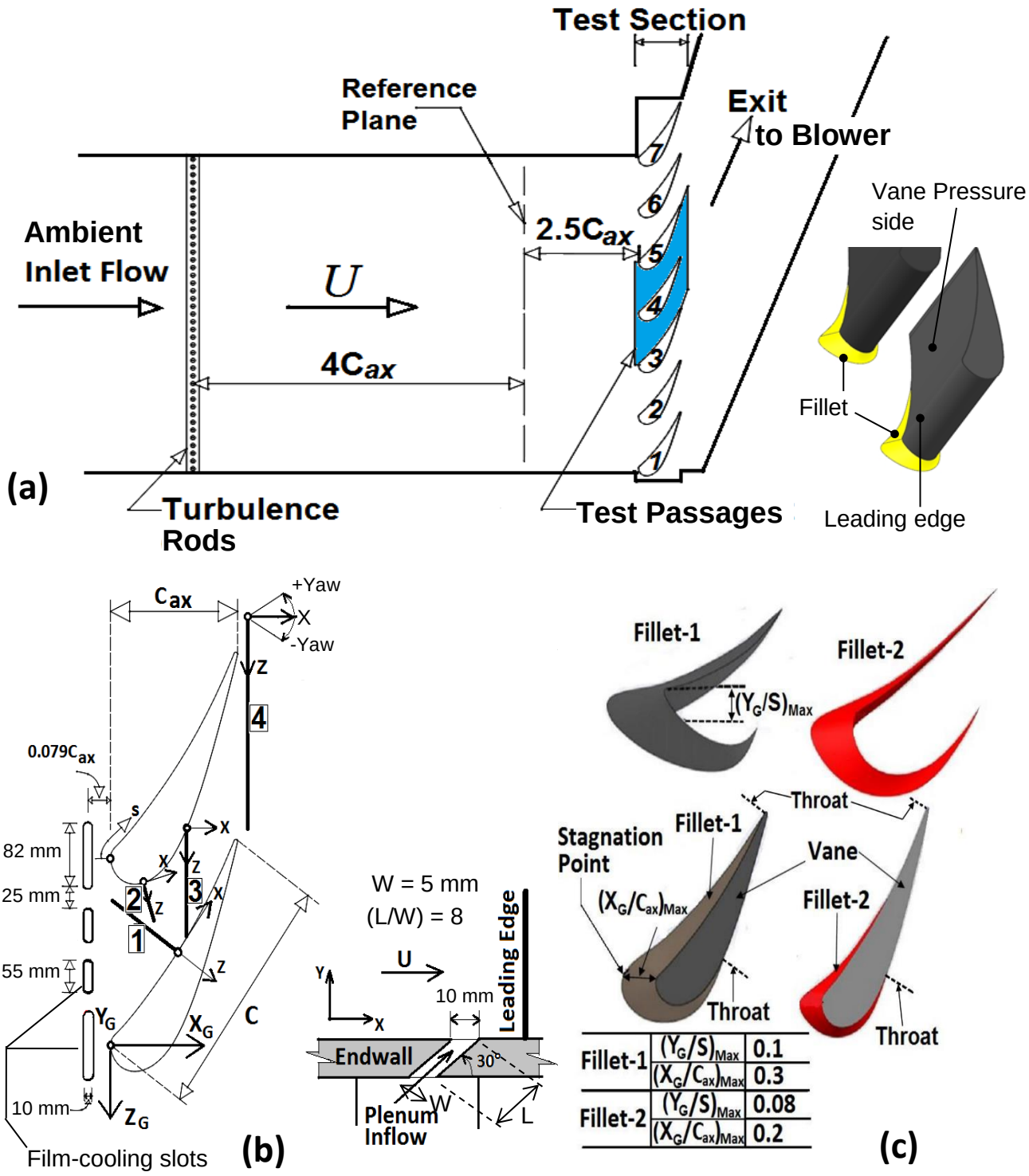

Figure 1: Schematics of experimental setup: (a) Wind tunnel and vane cascade (plan view); (b) Vane profile, coordinate systems, and measurement planes-(1 to 4) with film-cooling slot configurations; (c) Geometry of two fillets. Adopted from Mahmood and Arnachellan [28].

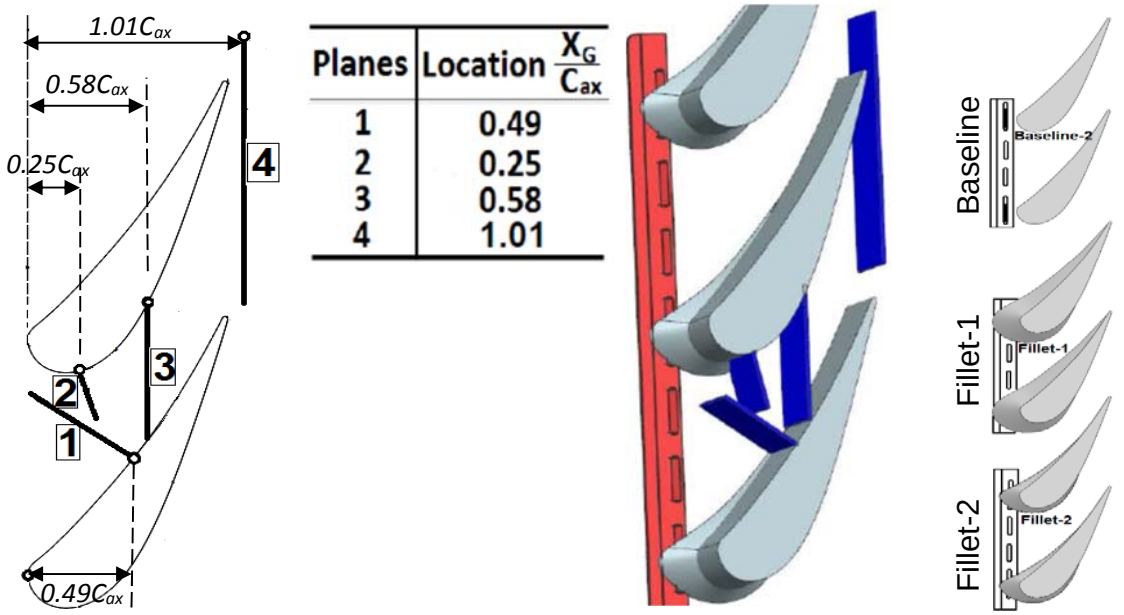

(a)

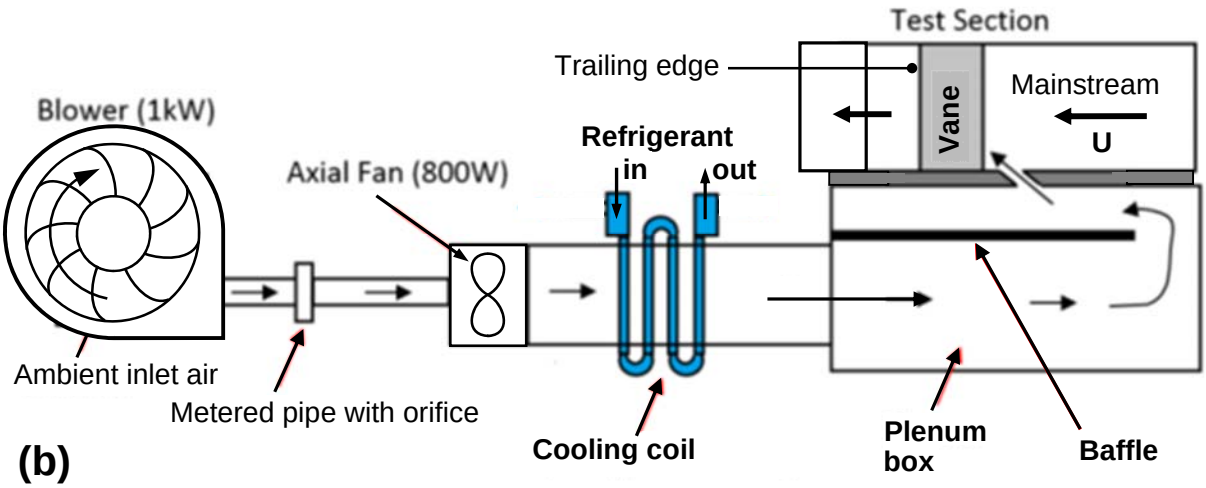

(b)

Figure 2: (a) Measurement planes with locations and upstream film-cooling configurations, and (b) Film-cooling flow circuit (adopted from Mahmood and Arnachellan [28]).

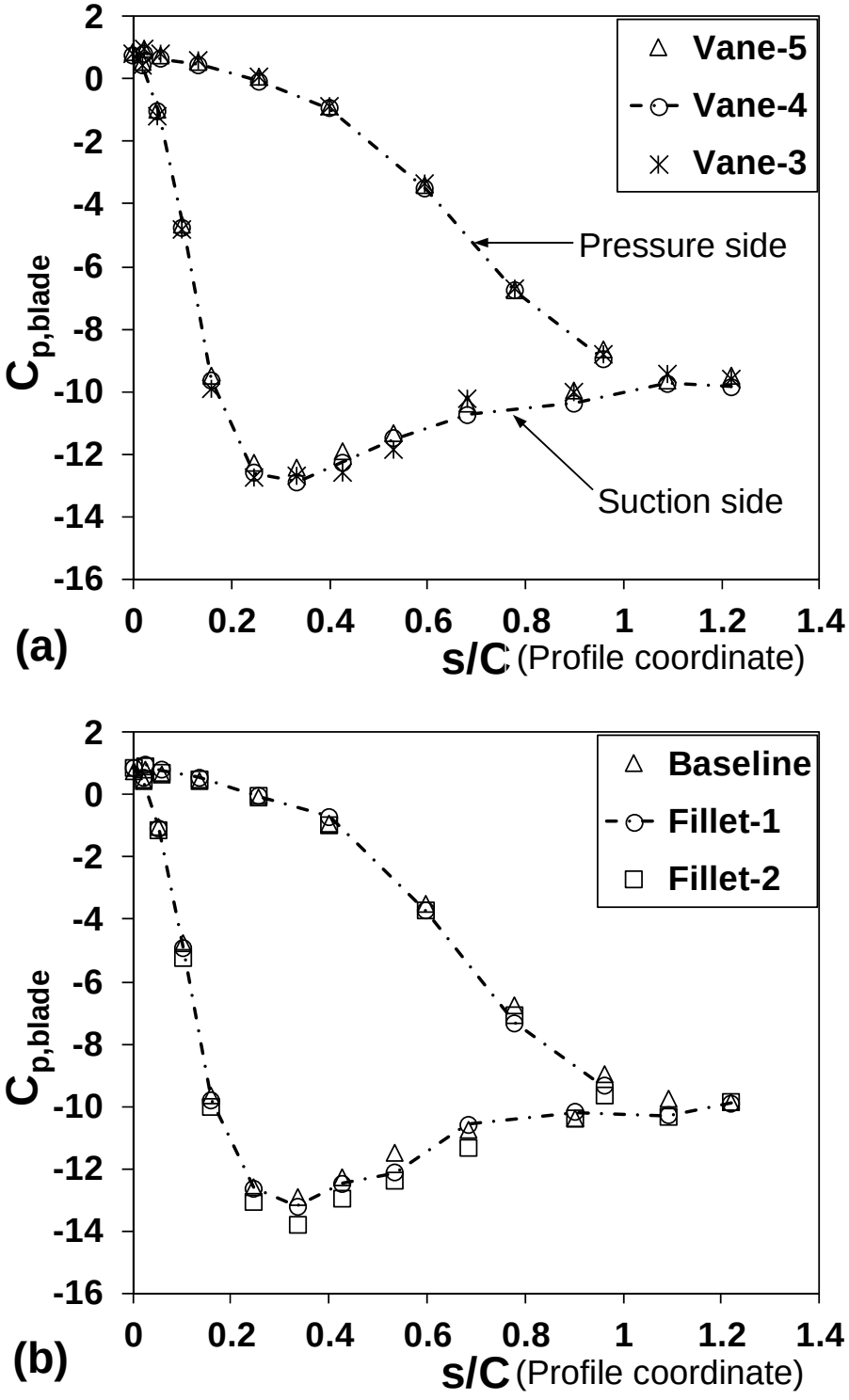

Figure 3: Static-pressure coefficient, $C_{p,blade}$ along vane profile at the mid-span location, Y_G/S = 0.5 with M_{in} = 0: (a) Vanes- 3, 4, 5; (b) Vane-4 (Baseline) and filleted vane-4 (Fillet-1, 2).

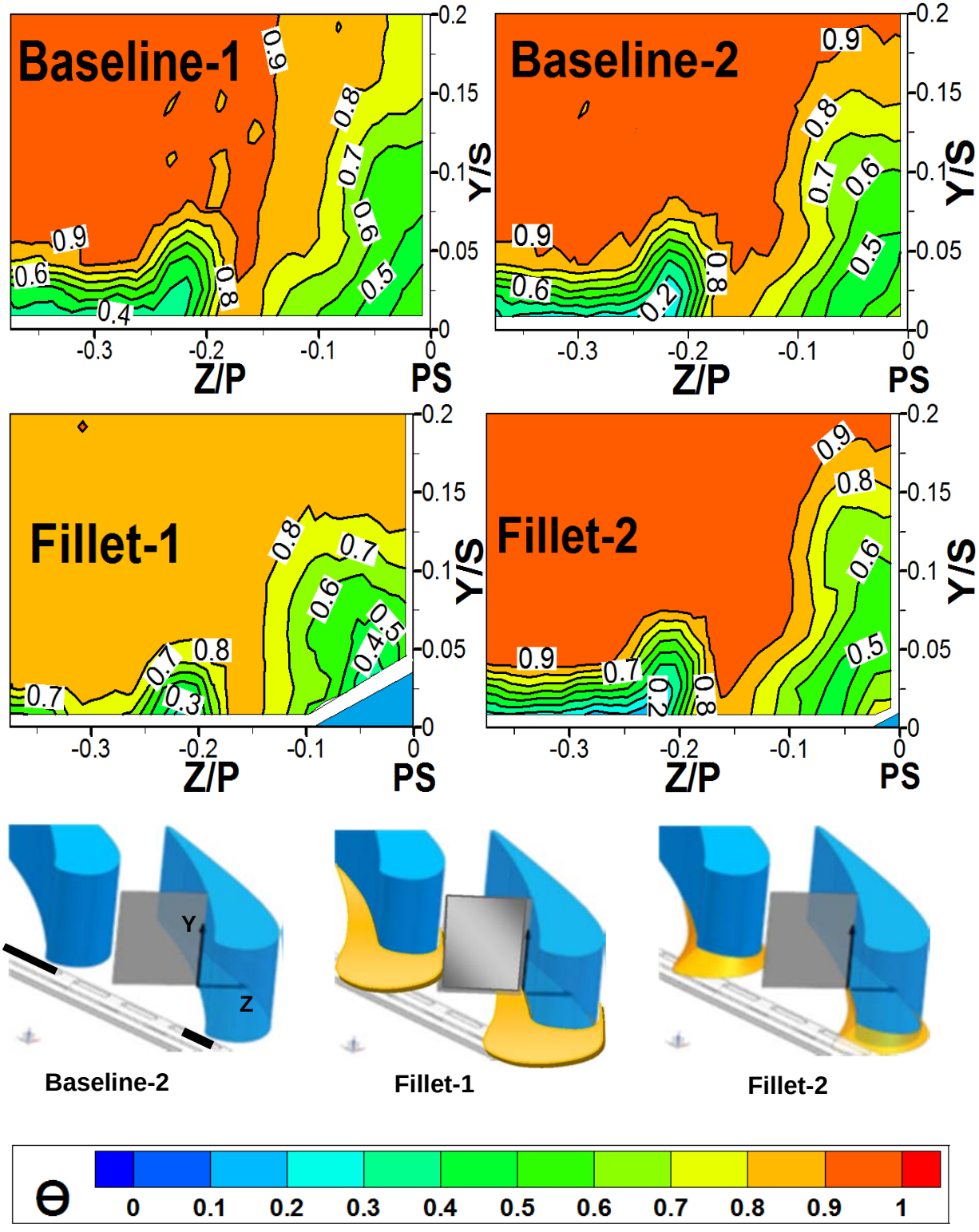

Figure 4: Distributions of non-dimensional temperature (θ) in plane-1 at X_G/C_{ax} = 0.49 for M_{in} =2.2 with and without fillets. Orientation of the plane and film cooling configurations are shown.

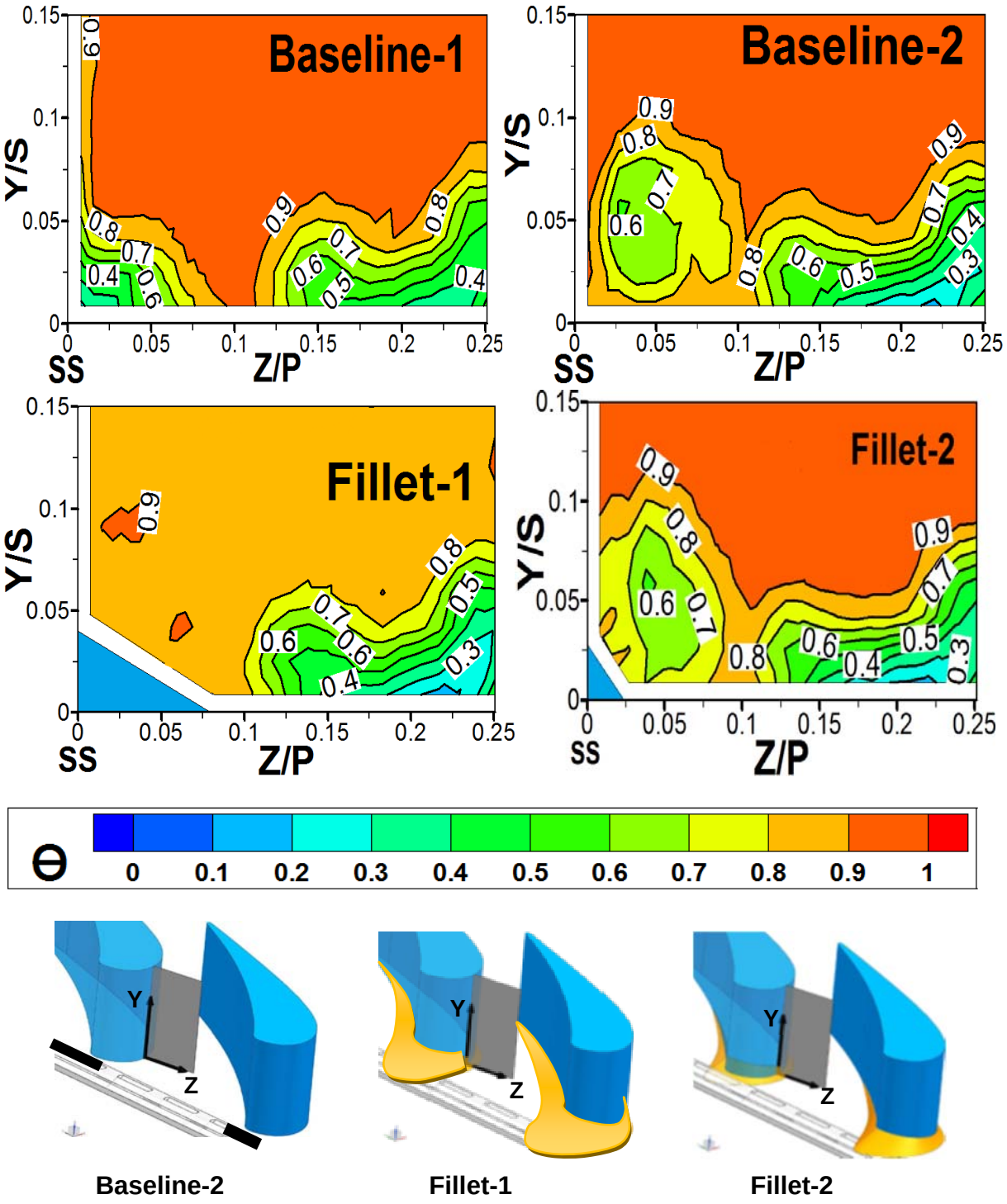

Figure 5: Distributions of non-dimensional temperature (θ) in plane-2 at X_G/C_{ax} = 0.25 for M_{in} =2.2 with and without fillets.

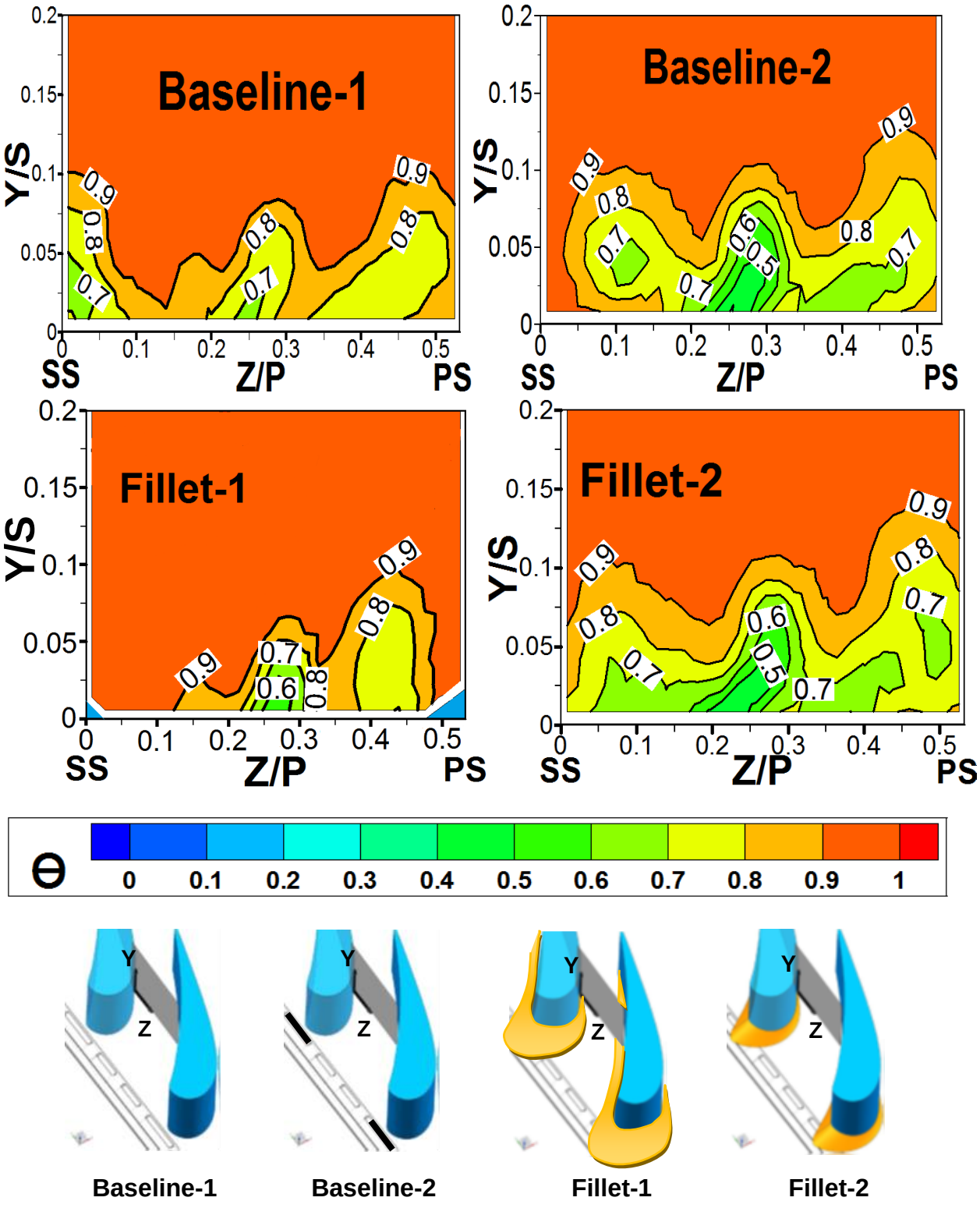

Figure 6: Distributions of non-dimensional temperature (θ) in plane-3 at X_G/C_{ax} = 0.58 for M_{in} =1.4 with and without fillets.

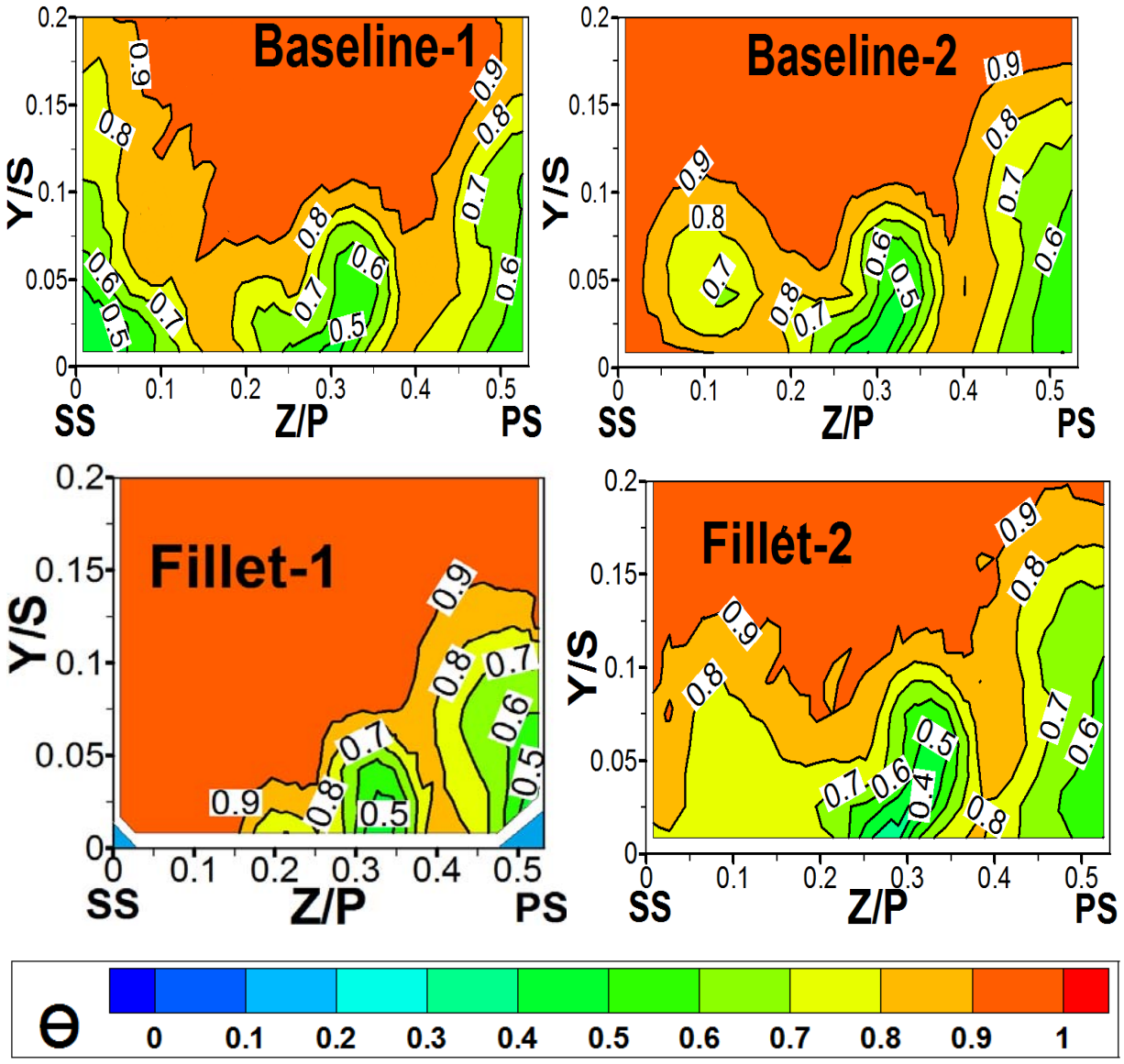

Figure 7: Distributions of non-dimensional temperature (θ) in plane-3 at X_G/C_{ax} = 0.58 for M_{in} =2.2 with and without fillets.

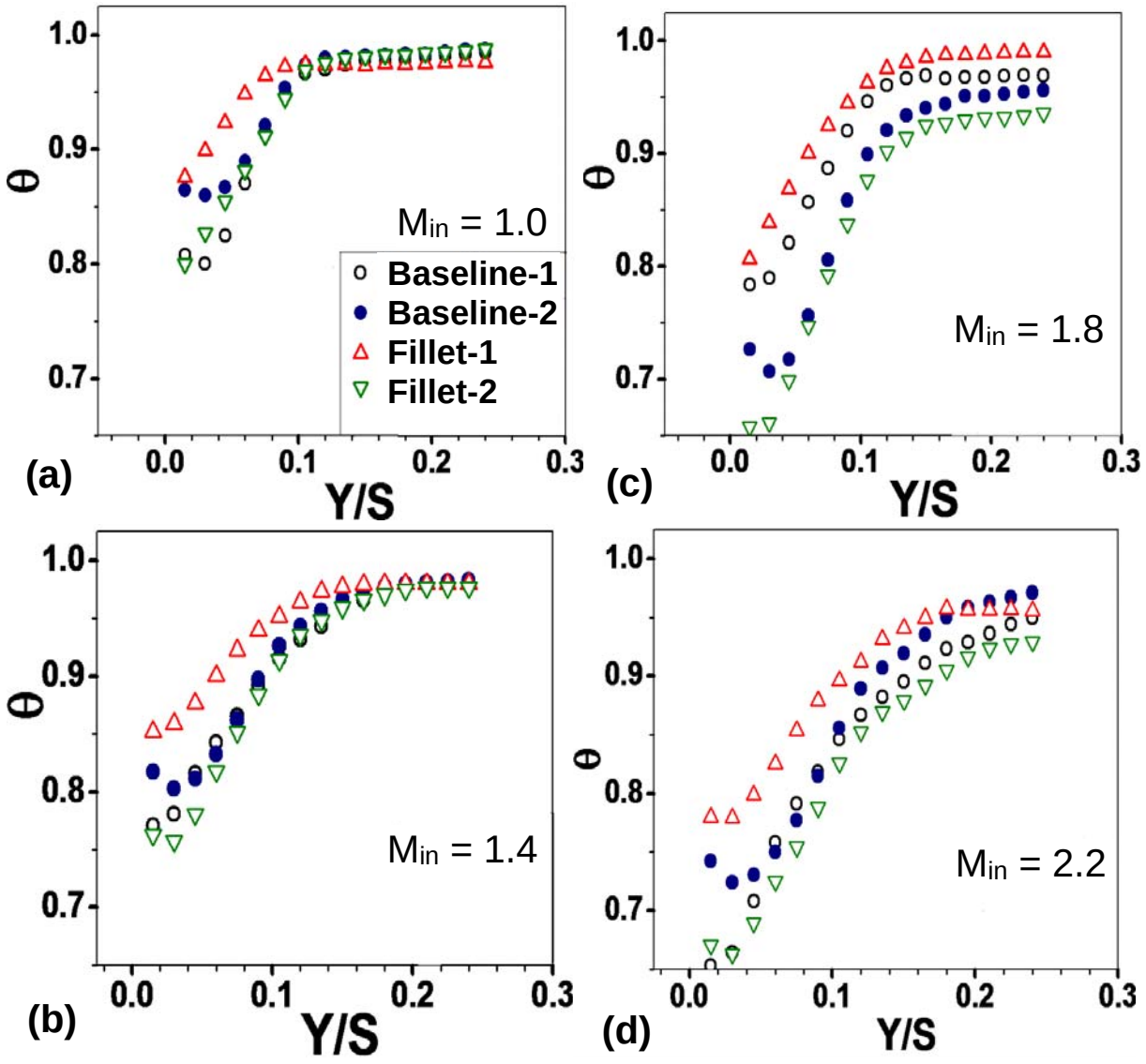

Figure 8: Pitchwise-average of non-dimensional temperature (θ) along spanwise Y/S in plane-3 at X_G/C_{ax} = 0.58: (a) M_{in} = 1.0; (b) M_{in} = 1.4; (c) M_{in} = 1.8; (d) M_{in} = 2.2. Legends are shown in Fig. 8(a).

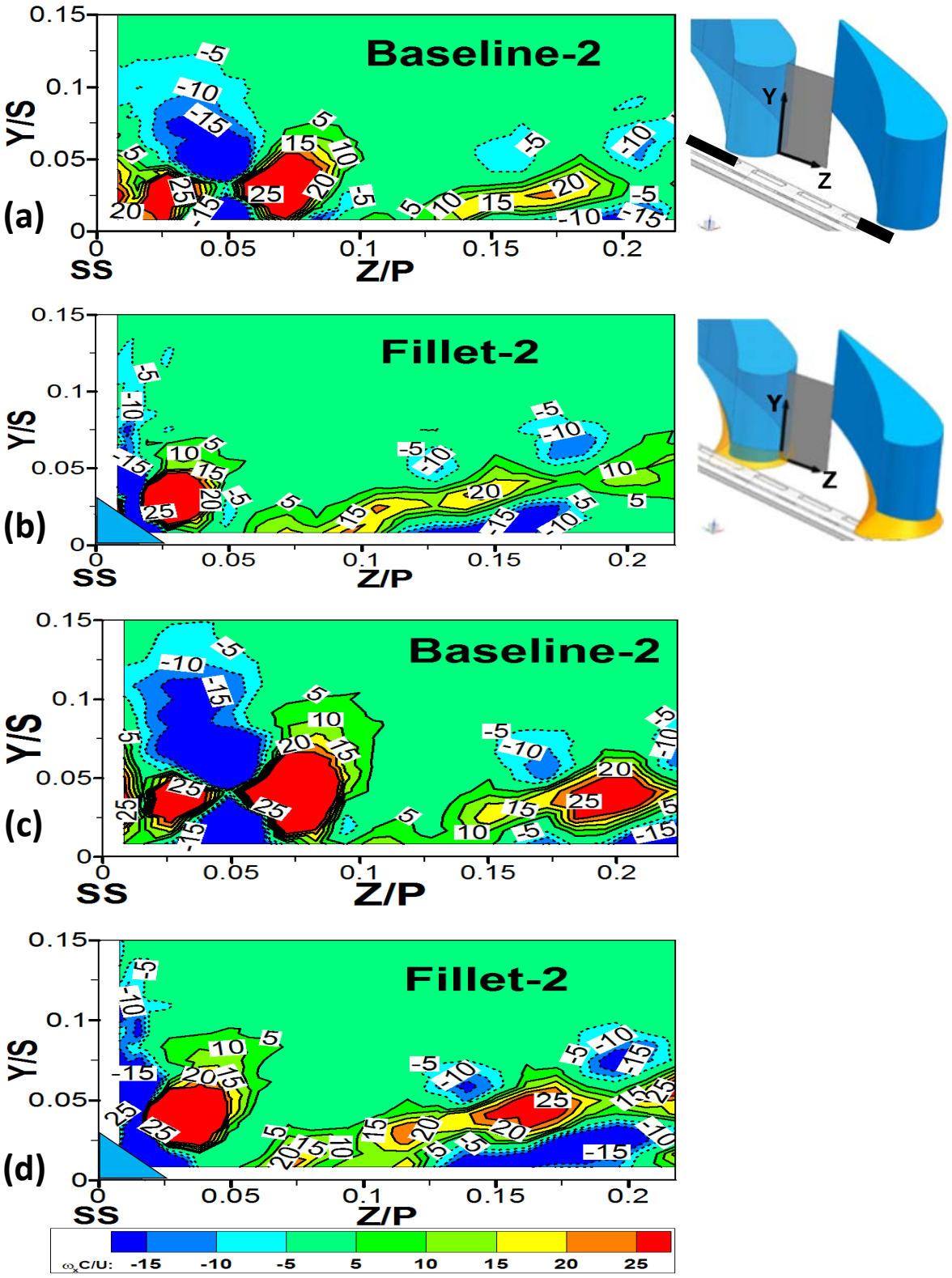

Figure 9: Distributions of normalized axial vorticity, $\omega_x C/U$ in plane-2 at X_G/C_{ax} = 0.25: (a) Baseline-2, M_{in} = 1.4; (b) Fillet-2, M_{in} = 1.4; (c) Baseline-2, M_{in} = 2.2; (d) Fillet-2, M_{in} = 2.2.

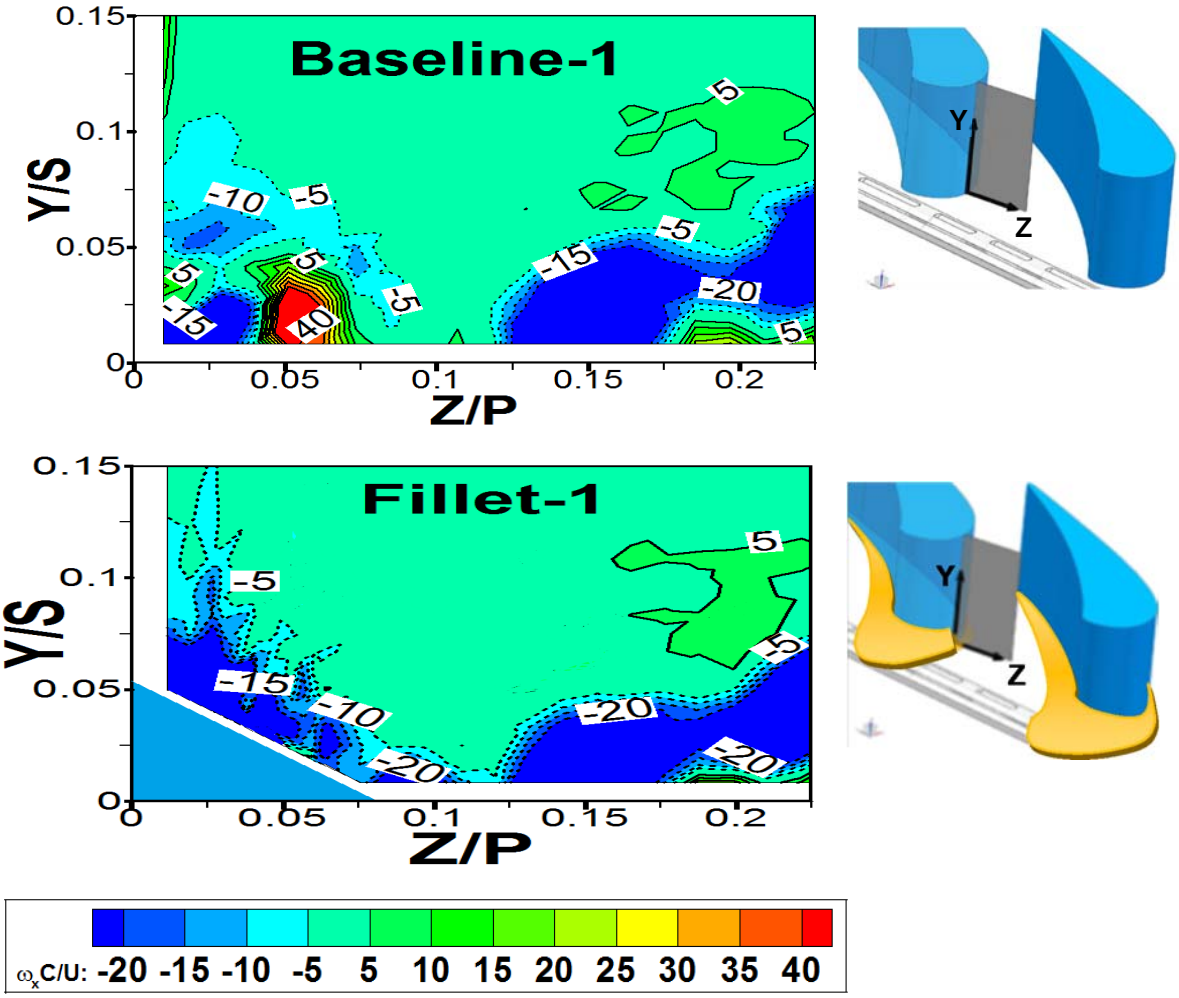

Figure 10: Distributions of normalized axial vorticity, $\omega_x C/U$ in plane-2 at $X_G/C_{ax} = 0.25$ for $M_{in} = 2.2$ with configurations of Baseline-1 and Fillet-1.

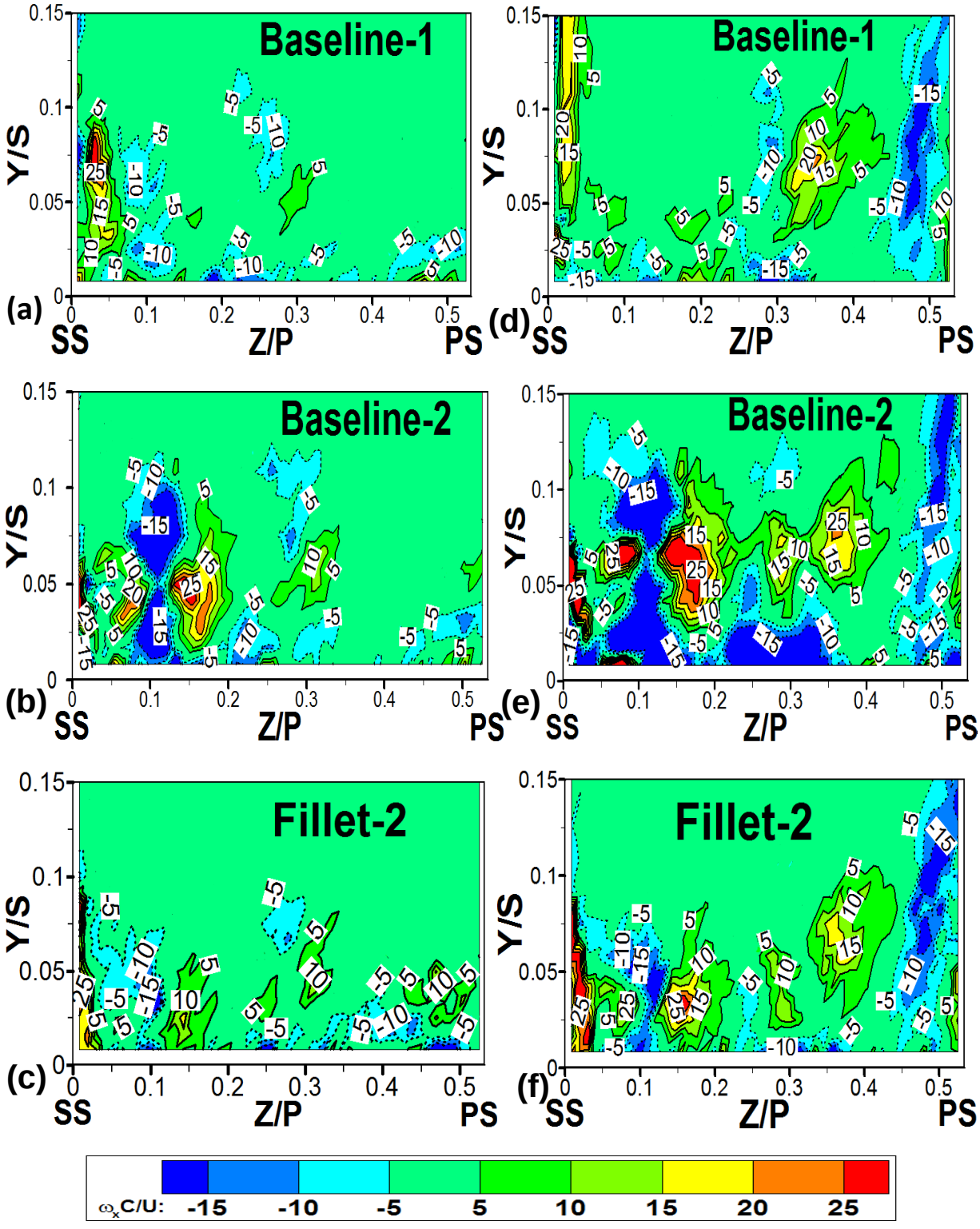

Figure 11: Distributions of normalized axial vorticity, $\omega_x C/U$ in plane-3 at X_G/C_{ax} = 0.58: (a) Baseline-1, M_{in} = 1.4; (b) Baseline-2, M_{in} = 1.4; (c) Fillet-2, M_{in} = 1.4; (d) Baseline-1, M_{in} = 2.2; (e) Baseline-2, M_{in} = 2.2; (f) Fillet-2, M_{in} = 2.2.

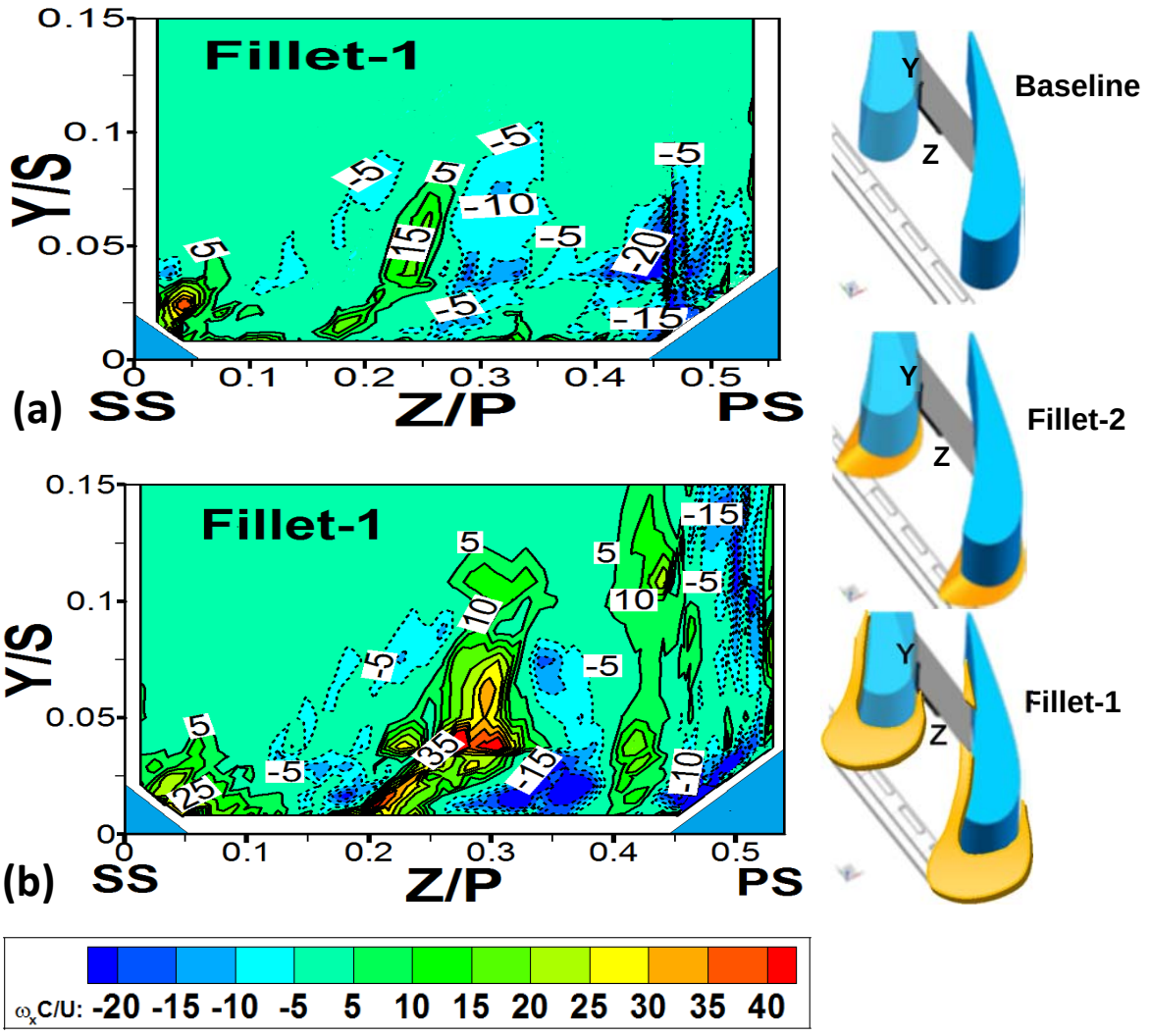

Figure 12: Distributions of normalized axial vorticity, $\omega_x C/U$ for Fillet-1 in plane-3 at X_G/C_{ax} = 0.58: (a) M_{in} =1.4; (b) M_{in} =2.2.

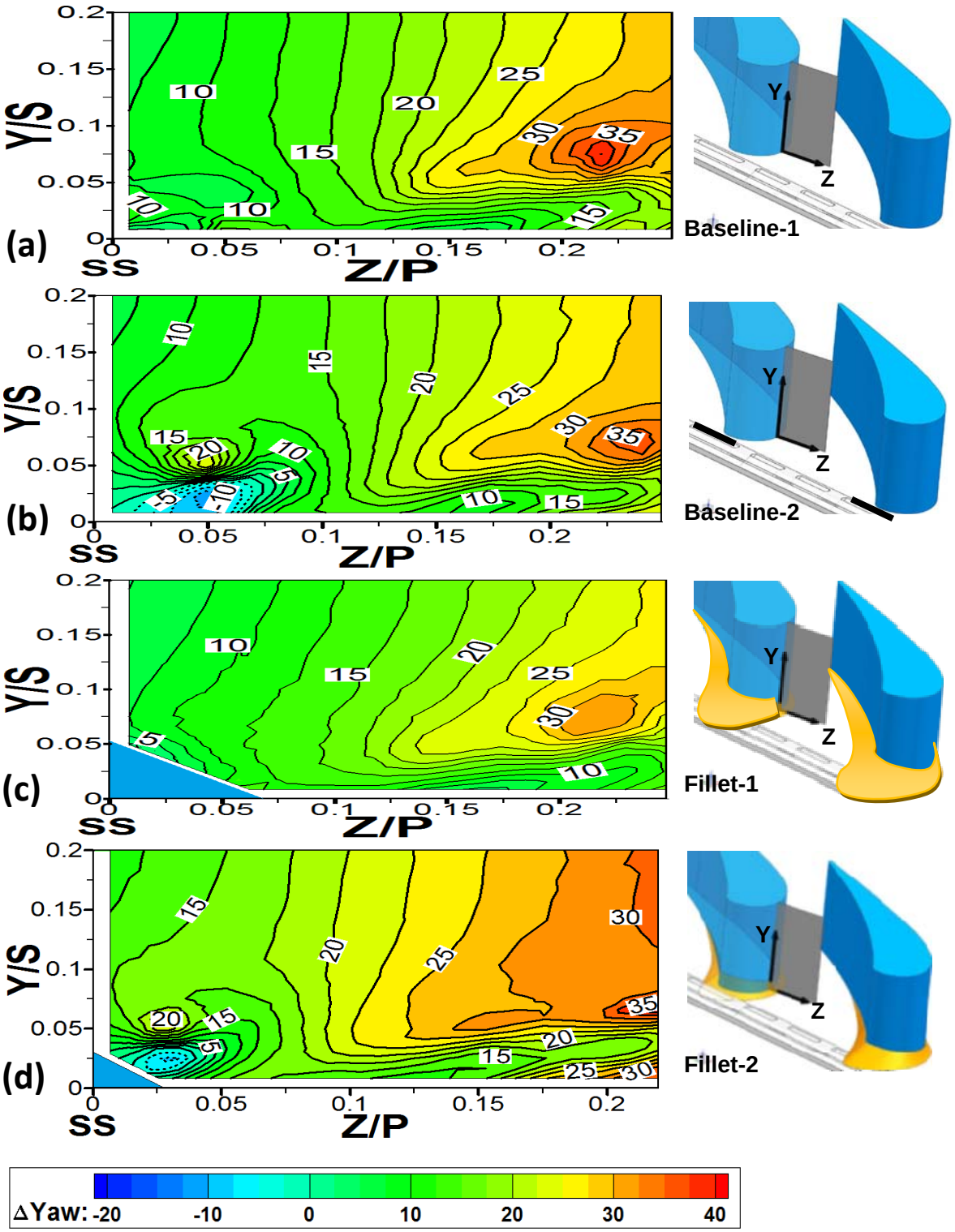

Figure 13: Distributions of yaw angle deviation, ΔYaw in plane-2 at X_G/C_{ax} = 0.25 for M_{in} = 2.2: (a) Baseline-1; (b) Baseline-2; (c) Fillet-1; (d) Fillet-2.

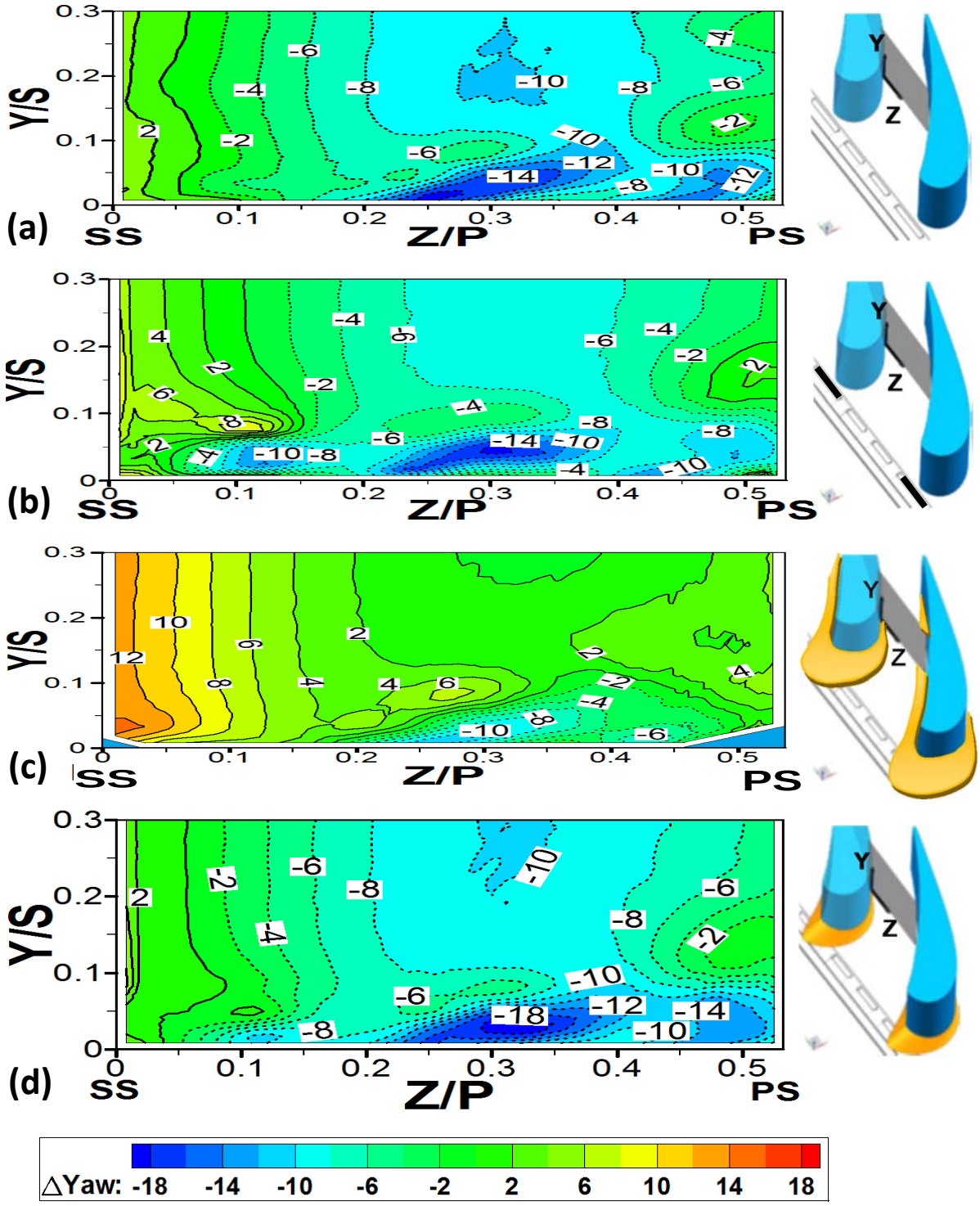

Figure 14: Distributions of yaw angle deviation, ΔYaw in plane-3 at X_G/C_{ax} = 0.58 for M_{in} = 2.2: (a) Baseline-1; (b) Baseline-2; (c) Fillet-1; (d) Fillet-2.

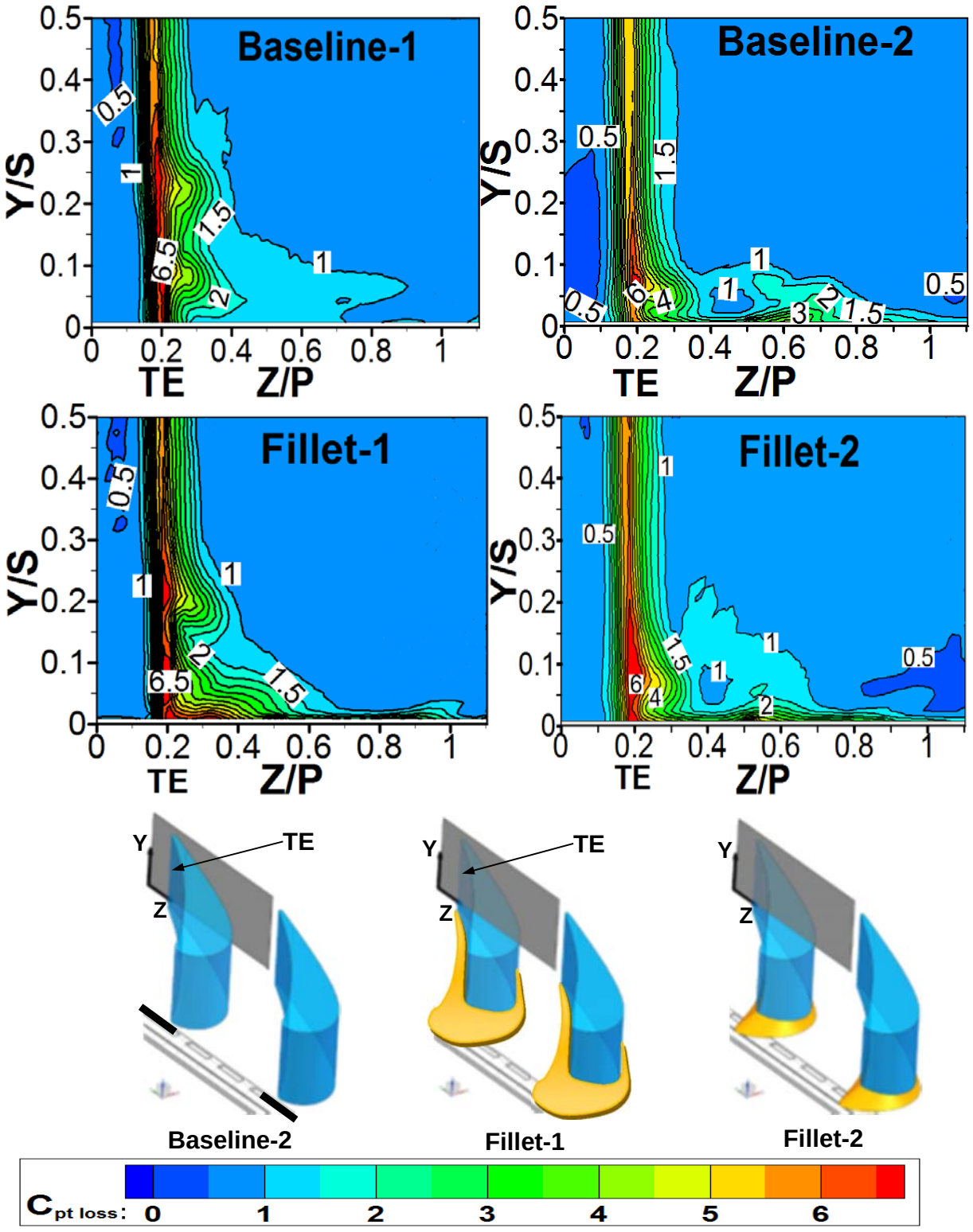

Figure 15: Distributions of total pressure loss coefficient, $C_{pt,loss}$ in plane-4 at X_G/C_{ax} = 1.01 for M_{in} =2.2 with and without fillets. Magnitude interval of contour values is 0.5.

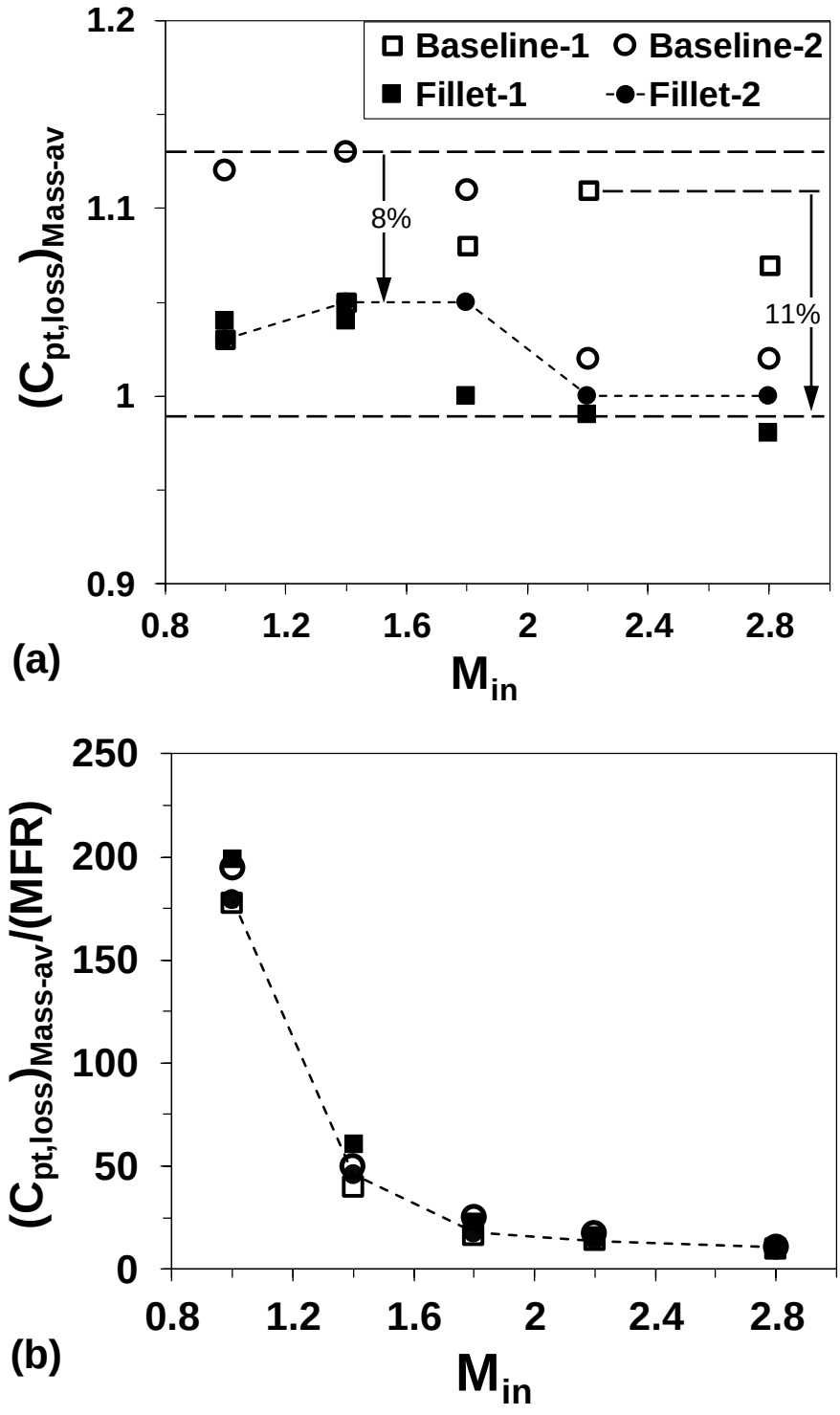

Figure 16: (a) Mass-averaged $(C_{pt,loss})_{Mass\text{-}av}$ and (b) mass-averaged $(C_{pt,loss})_{Mass\text{-}av}$ per unit mass fraction ratio (MFR) of film-cooling flow in plane-4 with and without fillets. Legends are shown in Fig. 16(a).